Comparative analysis of rhesus macaque and human placental organoids highlights evolutionary differences in placentation

Allyson Caldwell[1], Liheng Yang[1], Elizabeth A. Scheef[2], Amitinder Kaur[2], Carolyn B. Coyne*[1,3]

1 Duke University School of Medicine, Department of Integrative Immunobiology, Durham, NC
2) Tulane National Primate Research Center, Tulane School of Medicine, Covington, LA, 70433, USA.
3) Duke Human Vaccine Institute, Durham, NC

*Address correspondence:
Carolyn Coyne, PhD
3130 Medical Sciences Research Building III
3 Genome Court
Durham, NC 27710
USA
carolyn.coyne@duke.edu

Abstract

Throughout evolution, the placenta has diversified in structure and cellular composition while maintaining its essential role in supporting fetal development. Trophoblasts, key cells responsible for nutrient exchange and immune modulation, are a conserved feature of all placentas. Although primate placentas share broad morphological similarities, species-specific differences in gene expression remain poorly characterized, largely due to the lack of tractable *in vitro* models. To address this gap, we developed rhesus macaque placental organoids representing both trophoblast and maternal-derived decidual cell types and compared them with human placental organoids. Using integrated single-cell and single-nucleus RNA sequencing, we identified both shared and species-specific transcriptional programs across corresponding trophoblast lineages. We further reconstructed lineage trajectories leading to multinucleated syncytiotrophoblast and invasive extravillous trophoblast populations, revealing conserved differentiation pathways alongside divergent gene expression signatures. This work establishes new *in vitro* models of the nonhuman primate placenta and defines the molecular distinctions between human and rhesus trophoblasts, offering insights into the evolutionary adaptations underlying placental development.

Introduction

The placenta forms the critical interface between mother and fetus during pregnancy, providing both nourishment and protection to the developing fetus. In hemochorial placentas, fetal trophoblast cells are in direct contact with maternal blood. Trophoblasts are essential for proper placental development and function, playing key roles in nutrient exchange, hormone production, and immune modulation. In hemochorial mammals such as humans and rhesus macaques, the trophoblast-derived chorion fuses with the allantois, an extra-embryonic membrane originating from the embryonic hindgut, to form the chorioallantoic placenta. As the chorioallantoic placenta has evolved, trophoblasts have been conserved over time[1] and now include a variety of trophoblast populations. In most hemochorial mammals, these populations include cytotrophoblasts (CTBs) that can differentiate into other trophoblast subtypes including extravillous trophoblasts (EVTs) and the syncytiotrophoblast (STB). EVTs are located at the villous columns and invade into the decidualized endometrium where the placenta is attached during pregnancy. In early stages of gestation, EVTs remodel the maternal microvasculature to facilitate the entry of maternal blood into the intervillous space. The STB is the multinucleated trophoblast monolayer covering the surface of the hemochorial placenta and is formed by the fusion of mononuclear CTBs. While the overall architecture and trophoblast subtypes are conserved, key differences exist between species. For example, the extent and pattern of EVT invasion into the maternal decidua differs between humans and rhesus macaques[2]. These species-specific features underscore the importance of comparative models to study the maternal-fetal interface. The cellular heterogeneity and complexity of the placenta present a major challenge to accurately recapitulate placental biology *in vitro*, especially across species.

Rhesus macaques and humans develop morphologically similar placentas that contain comparable cell layers [3]. These similarities, along with the close evolutionary relationship between rhesus macaques and humans, make rhesus macaques an excellent research model to study human placentation and pregnancy. However, despite their similarities, previous studies have

53 identified key differences in the transcriptional signatures between rhesus macaque and human
54 trophoblasts[4]. For example, while human trophoblast populations express markers including HLA-
55 G, SIGLEC-6, and ERVW-1, these markers are absent in the rhesus macaque placenta[5-8].
56 Notably, these previous comparative studies were based on whole placental tissue rather than in
57 distinct trophoblast cell populations.

58 Organoids are three-dimensional models that recapitulate key features of their tissue of
59 origin, including cellular heterogeneity, organization, and function. Human trophoblast organoids
60 have been validated as a model that accurately recapitulates the cellular heterogeneity within the
61 human placenta and can be propagated and cryopreserved[9-11]. Our laboratory has previously
62 developed human trophoblast organoids (hTO) and decidua organoids (hDO) from full-term
63 placental tissue[11]. These organoids release pregnancy-associated hormones, differentiate to
64 contain key trophoblast subpopulations present in the human placenta, and accurately
65 recapitulate the transcriptional profile of trophoblasts observed *in vivo*[11,12]. Moreover, despite their
66 isolation from full-term tissue, hTOs more closely resemble trophoblasts in first-trimester
67 tissue[11,12]. These qualities make placental organoids a more physiologically relevant model than
68 other *in vitro* models, such as cell lines derived from choriocarcinomas. In addition to tissue-
69 derived organoids, trophoblast stem cells (TSC) have been developed as an *in vitro* model of both
70 human and rhesus macaque placentas[13,14]. TSC models consist of proliferative mononuclear
71 cytotrophoblasts that can differentiate to contain STB and EVT populations. While recapitulating
72 aspects of trophoblast biology, there are differences between tissue-derived TOs and TSCs, with
73 TSC-derived models lacking transcriptional signatures associated with trophoblast lineages[12,15,16].
74 Here, we developed rhesus macaque trophoblast organoids (rTO) and decidua organoids (rDO)
75 from matched late gestation placentas. Morphologically, rTOs and rDOs closely resembled
76 organoids derived from human tissue and expressed canonical markers of placental tissue.
77 Moreover, these organoids recapitulated the hormone release and transcriptional signature of
78 rhesus macaque placental tissue. We characterized the cellular heterogeneity of rTOs using

single-cell (sc) and single-nucleus (sn) RNA sequencing and compared their transcriptional profiles to those of hTOs. Using this approach, we defined the transcriptional signatures of distinct rhesus macaque trophoblast populations and identified shared and unique gene signatures in human trophoblasts. To model differentiation, we treated rTOs and hTOs with media conditions known to promote EVT formation. We then compared the trajectories of cytotrophoblast (CTB) differentiation into STB and EVT lineages across species, revealing conserved and divergent transcriptional programs associated within these trophoblast subtypes. Altogether, this work establishes new *in vitro* models of the rhesus macaque placenta, allowing for direct cross-species comparisons to model human and non-human primate placentation.

Results

Derivation of trophoblast and decidua organoids from rhesus macaque placentas

To generate matched trophoblast and decidua organoids, we dissected fetal and maternal tissues from mid-late third trimester gestation rhesus macaque placentas (143-154 gestational days) (**Figure 1A**). The architecture of chorionic villi is similar between rhesus macaque and human placentas, but rhesus macaques exhibit shorter, wider, and less branched villi than do humans (**Figure 1B**). To develop rhesus macaque trophoblast organoids (rTOs), we dissected the chorionic villi and smooth chorion and carefully removed any decidua tissue. The chorionic villi and smooth chorion were homogenized using similar protocols that were developed previously to isolate human trophoblast organoids (hTOs) from full-term placental tissue[11]. To develop rhesus decidua organoids (rDOs), we isolated progenitor cells from decidual glands, following a similar approach as described for human DOs (hDOs). Isolated progenitor cells from the fetal and maternal tissues were then cultured in Matrigel to develop rhesus macaque placental organoids. Rhesus-specific growth factors are not commercial available therefore, rhesus macaque placental organoids were grown in previously defined term trophoblast organoid media (TOM) used for hTOs . Organoids were visible ~5-7 days post-isolation and were passaged every ~7-10 days

105 (rTOs) or every ~5-7 days (rDOs) once established. Morphologically, rTOs and rDOs resembled
106 hTOs and hDOs (**Figure 1C**) and could be propagated long-term (>15 passages) without loss of
107 this morphology (**Figure 1D**). Confocal microscopy for cytokeratin-19 confirmed the architecture
108 of rhesus macaque organoids, which were similar to those derived from human placental tissue
109 **(Figure S1A-B, D)**. Collectively, these data demonstrate the successful derivation of rTOs and
110 rDOs from rhesus macaque placental tissue.
111

112 **Rhesus macaque-derived placenta organoids secrete pregnancy hormones and express**
113 **canonical markers**

114 To examine the localization of canonical trophoblast and decidua markers in rTOs and rDOs, we
115 performed immunostaining using cell-type specific markers. In rTOs, this included the STB marker
116 syndecan-1 (SDC-1) and the CTB marker integrin alpha-6 (ITGA6). rTOs and hTOs both
117 expressed SDC-1, indicating the presence of the fused STB and ITGA6 representing the
118 mononuclear CTBs **(Figure 1E and 1F, S1C).** Unlike hTOs, which develop with an inward facing
119 STB, SDC-1 localization suggested that rTOs developed with an outward facing STB **(Figure 1E**
120 **and 1F**, **Supplemental Movies 1 and 2)**. Additionally, rDOs expressed decidua gland-associated
121 markers including E-cadherin and the mucin MUC5AC, similar to their expression in hTOs **(Figure**
122 **1G and 1H, S1C)**.

123 Human TOs secrete essential pregnancy hormones including human chorionic
124 gonadotropin (hCG)[9,11]. During pregnancy, the rhesus macaque placenta secretes chorionic
125 gonadotropin (mCG) early in pregnancy with a peak occurring at approximately gestation day 22-
126 24[17]. In addition, progesterone is secreted during rhesus macaque pregnancy similar to human
127 pregnancy, with fluctuations throughout gestation[17]. Therefore, we investigated whether rTOs
128 secreted mCG and/or progesterone. To do this, we used two approaches including unbiased mass
129 spectrometry of conditioned medium (CM) collected from rTOs and an established
130 radioimmunoassay[18,19]. For mass spectrometry, we collected CM from three independent wells of

131 rTOs derived from two unique placentas and isolated bands migrating at ~26kD and ~10kD, the
132 approximate size of chorionic gonadotropin A (CGA), on a reducing SDS-PAGE gel (**Figure S1E**).
133 Spectral counts for CGA, which is secreted with CG beta subunits to form mCG, were detected
134 in every conditioned media (CM) sample isolated from rhesus trophoblast organoids (rTOs), with
135 high identification probability (**Figure 1I, 1J**). In contrast, no spectral counts for CGA mapped in
136 any non-conditioned medium (NCM) control samples (**Figure 1I, 1J**). To directly quantify the
137 levels of mCG and progesterone secreted from rTOs, we collected CM from three unique rTOs
138 lines and performed a radioimmunoassay described previously[18,19]. NCM controls were assayed
139 in triplicate and subtracted from rTO conditioned media samples. We found high levels of mCG
140 (>1000ng/mL) and progesterone (>1200ng/mL) in rTO conditioned media, **(Figure 1K)**. Similar to
141 hTOs, rTOs can be passaged long-term without loss of mCG or progesterone secretion.

142 Lastly, we performed bulk RNA sequencing of rTOs and rDOs to assess the expression of
143 known canonical markers of human trophoblasts or glandular epithelial cells, respectively, and to
144 verify the absence of contamination of other tissues/cells. To do this, we compared the expression
145 profile of canonical markers of rhesus-derived trophoblasts and decidua epithelial organoids. We
146 found that rTOs highly expressed trophoblast-specific markers, including *PGF*, *MMP2*, and *ITGA5*
147 which were absent or expressed at low levels in rDOs **(Figure S1F)**. We also found that rTOs
148 expressed markers of distinct trophoblast lineages including the STB (e.g., *CGA*), CTBs (e.g.,
149 *FOXO4*), and EVTs (e.g., *MAMU-AG*). Conversely, rDOs expressed markers associated with the
150 maternal decidua including *MUC1*, *MUC20*, and *SOX17*, which were absent or expressed at low
151 levels in rTOs **(Figure S1F, S1J)**. These results were similar to the differences observed between
152 hTOs and hDOs **(Figure S1G)**.

153 We next analyzed the transcriptional dataset to identify non-annotated genes associated
154 with rhesus macaque trophoblasts, which included pregnancy-specific glycoproteins (PSGs).
155 PSGs have been described in many non-human species, including primates, mice, horses, and
156 cows[20]; however, the driving forces of evolution of these genes is unclear. Rhesus macaque PSGs

157 have not been annotated with gene names in the recent *Macaca Mulatta* genome assembly (
158 Mmul10). We identified rhesus macaque PSGs in the rTO dataset by comparing the genome
159 sequence of unannotated macaque genes to the human genome (hg38) using BLAST. We
160 identified rhesus macaque PSGs in the rTO dataset by comparing the genome sequences of
161 unannotated macaque genes to the human reference genome (hg38) using BLAST. This analysis
162 revealed five PSGs that were expressed in rTOs (**Figure S1H**). In comparison, ten PSGs were
163 expressed in hTOs based on annotations in the human genome (**Figure S1I**). Together, these
164 data demonstrate that rTOs and rDOs recapitulate key aspects of the rhesus macaque placental
165 transcriptome, including the expression of cell type–specific markers.

166 To characterize the transcriptional profiles of rhesus TOs and DOs, we performed
167 differential gene expression analysis using edgeR to identify genes distinguishing these organoid
168 types (**Figure S1J**). This analysis revealed distinct expression profiles between rTOs and rDOs.
169 To confirm the identity of decidual organoids, we also conducted signature scoring using a curated
170 set of glandular epithelial markers, which demonstrated robust expression of decidual-associated
171 genes in rDOs (**Figure S1K**). We next compared gene expression profiles between rDOs and
172 hDOs using edgeR to identify both species-specific and conserved transcriptional signatures
173 (**Figure S1L**). This analysis revealed clear divergence in gene expression patterns between
174 species. Notably, *TRIM72* and *PARP6* were significantly upregulated in rDOs, while *OST4* and
175 *EMC4* showed higher expression in hDOs, underscoring species-specific molecular programs
176 within decidual tissues. Additional differentially expressed genes included cytokines,
177 mitochondrial components, and transcriptional regulators, reflecting both functional specialization
178 and evolutionary divergence. To investigate the functional relevance of genes conserved between
179 rDOs and hDOs, we performed gene ontology (GO) enrichment analysis using the clusterProfiler
180 algorithm (**Figure S1M**). This analysis revealed significant enrichment in pathways related to
181 olfactory receptor activity, DNA-binding transcription activator activity, cytokine activity, and
182 receptor ligand activity. These findings emphasize both the evolutionary conservation and

183 divergence of decidual biology across primates and support the utility of the rDO model for cross-
184 species comparisons.
185

186 **Single-cell RNA-seq mapping of rTOs reveals comparable cellular heterogeneity to hTOs**

187 To evaluate whether rTOs mirror the cellular heterogeneity of the rhesus placenta, we performed
188 single-cell RNA sequencing (scRNAseq) on rTOs cultured under standard conditions. In parallel,
189 we generated new scRNAseq data from hTOs and incorporated previously published datasets
190 from our prior work[12]. Established lines of rTOs and hTOs were dissociated into single cell
191 suspensions and processed separately to identify cell types present in TOs. A total of 11,916
192 (rTOs) and 15,766 (hTOs) cells passed quality control and were used for cluster analysis and cell-
193 type specific marker expression analysis following integration to correct for batch effects.
194 Clustering analysis revealed five major cell populations present in both rTOs and hTOs (**Figure**
195 **2A**, **2B**) which were distributed similarly across all TO lines (**Figure 2C, 2D, S2A, S2B**). To define
196 the cellular identity of each cluster, we identified cluster-enriched gene expression profiles and
197 mapped them to canonical trophoblast markers[4,14]. Clusters in rTOs included two non-proliferative
198 CTB populations (CTB-1 and -2) which accounted for ~31% and ~20% of all populations
199 respectively, two proliferating CTB populations (CTBp-1 and -2) which accounted for ~24% and
200 ~23%, and one STB cluster which only accounted for 2% (**Figure 2A, 2C**). Given the
201 multinucleated nature of the STB, it is less represented in scRNAseq datasets from both tissue
202 and TOs[12]. CTB clusters were enriched in canonical markers including *KRT7* and *CDH1* whereas
203 CTB-p clusters were enriched in genes associated with proliferation (e.g., *MKI67*, *CCNA2*)
204 (**Figure 2E, 2G**). The STB cluster was enriched in canonical markers including *TFAP2A*, *INSL4*,
205 *HOPX*, *CGA*, and the endogenous retrovirus fusion gene *ERVFRD-1* (**Figure 2E, 2G**). Many
206 genes previously identified in TSC-derived rhesus macaque lineages[14] to be expressed in CTBs
207 (**Figure S2C**) and STB/EVTs (**Figure S2D**) were also expressed in a lineage-specific manner.
208 Unbiased cluster gene enrichment analysis also demonstrated that as expected, both CTB-p

clusters were enriched for genes associated with cell division (e.g., *CENPF*, *CCNB1*) and histones (e.g., *H1-5*, *H1-3*) (**Figure S2E**). In contrast, the CTB-1 cluster in rTOs was enriched in gene associated with extracellular matrix (e.g., *LAMB3*, *LAMC2*) and the regulation of MMPs (e.g., *TIMP1*, *TIMP3*) whereas CTB-2 was enriched in genes associated with GTPases and GTP-binding proteins (e.g., *ARL15*, *AGAP1*) and NOTCH signaling (e.g., *MAML2*, *MAML3*) (**Figure S2E**). These expression profiles were distinct from genes enriched in the STB, which included canonical markers (e.g., *HOPX*, *CGA*) and several non-annotated genes (e.g., *ENSMMUG00000049714*, *ENSMMUG00000063643*) (**Figure S2E**). Many of the non-annotated STB-enriched genes are predicted to encode for rhesus macaque CGBs (*ENSMMUG00000040968, ENSMMUG00000063643, ENSMMUG00000049714*) and PSGs as we described above (*ENSMMUG00000039210, ENSMMUG00000050799, ENSMMUG00000047533*) (**Figure S2F, S2G**). Previous studies described the expression of CGBs in macaque trophoblast stem cell lines[14,21] but these studies did not state which specific CGBs were present. The GO terms and genes associated with population-specific trophoblast-enriched genes included the regulation of cell locomotion, motility, and migration, actin cytoskeletal organization and processes (e.g., *ACTG1*, *PFN1*, *CDC42*) in CTB-1 whereas those associated with CTB-2 were involved in the regulation of GTPase and hydrolase activities (e.g., *RGL1*, *SNX13*, *RALGPS2*, *ARFGEF1*) (**Figure S2H, S2I**). These pathways and genes were distinct from the STB, in which pathways including protein catabolic processes and endomembrane system organization were enriched (e.g., *FOLRF1*, *EHD3*, *RAB11A*) (**Figure S2H, S2I**). STB-associated GO terms and associated genes included catabolic processes, synaptic vesicle maturation, and protein localization to the plasma membrane (**Figure S2H, S2I**). These data highlight the distinct cellular processes and functions amongst distinct rhesus macaque trophoblast populations in rTOs.

Clusters in hTOs included two non-proliferative CTB populations (CTB-1 and -2) which accounted for ~24% and ~15% of all populations respectively, two proliferating CTB populations

235 (CTBp-1 and -2) which accounted for ~27% and ~24%, and one STB cluster which only accounted
236 for 8% (**Figure 2B, 2D**). Gene enrichment in hTOs was similar to rTOs, with pCTBs highly
237 enriched for markers of proliferation (e.g., *MKI67* and *CCNA2*), CTBs enriched for canonical
238 markers (e.g., *KRT7* and *CDH1*), and the STB enriched for canonical marker (e.g., *TFAP2A,*
239 *INSL4, HOPX, ERVW-1*, and *CYP19A1*) **(Figure 2F, 2H)**. Also, like rTOs, one CTB cluster, CTB-
240 2, expressed markers of undifferentiated EVTs including *ITGB1* and expressed low levels of the
241 canonical EVT marker *HLA-G* (**Figure 2F**). Collectively, these data define the cellular composition
242 of rhesus macaque- and human derived-trophoblast organoids and show that these organoids
243 differentiate into multiple trophoblast lineages.
244

245 **Defining trophoblast marker divergence and convergence in rTOs and hTOs**

246 Next, we integrated scRNAseq datasets from rTOs and hTOs to perform evolutionary gene
247 expression analysis, aiming to identify both divergence and convergence in cell marker
248 expression between the two species. This analysis revealed five conserved clusters, most of
249 which were comprised of near-equivalent ratios of rTO- and hTO-derived cells (**Figure 3A**, **3B**).
250 These populations were conserved across independent rTO and hTO lines (**Figure S3A**).
251 Clusters expressed canonical markers of CTB-p (e.g., *MKI67*, *TOP2A*), CTBs (e.g., *CDH1*,
252 *KRT7*), and the STB (e.g., *TFAP2A*, *HOPX*) (**Figure 3C**). Expression of these canonical markers
253 was conserved in both rTO and hTO datasets (**Figure 3D**). Unbiased gene enrichment analysis
254 identified select genes defining two CTBp clusters (CTBp-1, CTBp-2), two CTB clusters (CTB-1,
255 CTB-2) and a single STB cluster (**Figure S3B**). We did not observe distinct EVT clusters in the
256 combined dataset but select clusters did express both rhesus macaque and human EVT markers
257 **(Figure S3C)**. We performed gene ontology enrichment analysis, using the *clusterProfiler*
258 algorithm, on rhesus macaque and human datasets and identified molecular function pathways
259 uniquely enriched in each (**Figure S3D, 3E, 3F)**. Next, we investigated the transcriptional profiles
260 of the CTBp and CTB clusters (**Figure S3G–J**). Notably, we found that CTBp clusters exhibited a

261 higher degree of transcriptional conservation across species, with a greater proportion of shared
262 marker genes compared to CTB clusters. This suggests that the proliferative state of
263 cytotrophoblasts may be governed by more conserved regulatory programs, whereas non-
264 proliferative CTBs may exhibit greater species-specific variation in gene expression.

265 We next focused on differential gene expression within the STB cluster between rTOs and
266 hTOs. While this cell type is conserved across species, the extent to which its transcriptional
267 profile diverges remains largely unknown. We found that there was near-equivalent expression of
268 canonical STB genes including *HOPX*, *INSL4*, *CGA*, in both rTOs and hTOs (**Figure 3E**). We also
269 observed the expression of orthologs in the STB cluster, including genes such as CGBs and PSGs
270 that were expressed at similar levels in both rTOs and hTOs (**Figure 3F**). To elucidate differences
271 in the transcriptional profiles of the STB markers rTOs and hTOs, we performed pseudobulk
272 differential expression analysis using DESeq2. This analysis identified differences in STB-
273 associated transcriptional profiles and highlighted variations in gene expression arising from
274 differences in annotation and/or gene presence between the human and rhesus genomes **(Figure**
275 **3G)**. Of the STB markers in the integrated dataset, 15.1% were shared between the two species
276 **(Figure 3G)**. These markers included calpain-6 (*CAPN6*), inhibin subunit alpha (I*NHA*), and
277 *ERVFRD-1* (**Figure 3H**). rTO-specific STB markers accounted for 48.4% of the STB markers and
278 27.3% of these genes were found only in the rhesus macaque genome (**Figure 3G**). hTO-specific
279 STB markers made up 36.6% of the STB markers and 25.9% of these markers were found only
280 in the human genome (**Figure 3G**). We therefore focused on defining gene expression
281 conservation and variance from genes conserved in both genomes. This analysis revealed
282 significant differences in STB marker expression between rTOs and hTOs. For example, the STB
283 in rTOs expressed the peptide hormone corticotropin-releasing hormone (*CRH*), the transcription
284 factor *ELF4*, and the cytokeratin *KRT81*, amongst others (**Figure 3I, 3J**). In contrast, hTOs were
285 enriched in genes including *CYP19A1*, the endogenous retrovirus gene *ERVV-1*, and the
286 chemokine *CCL5* (**Figure 3K, 3L**). These data demonstrate that although rTOs and hTOs share

key markers within their STB cells, each also exhibits species-specific gene expression signatures within this specialized cell type.

Single-nucleus RNA Sequencing Expands Resolution of Trophoblast Cell States in rTOs

Using scRNAseq, we identified both shared and species-specific features of STB cells in rTOs and hTOs. However, prior studies have shown that snRNAseq is essential for accurately capturing gene expression in the STB, due to their multinucleated nature and the limitations of scRNAseq in profiling such cells[12,16]. Therefore, to further characterize the specialized trophoblast populations in rTOs and their transcriptional profiles, we performed snRNAseq on rTOs. Three lines of rTOs were dissociated into single cell suspensions and nuclei isolated. To compare trophoblast populations captured by the two sequencing modalities, we integrated rTO scRNAseq and snRNAseq datasets (**Figure 4A**). This integrated dataset revealed that, consistent with previous studies in hTOs[12], scRNAseq of rTOs captured fewer STB-associated cells than snRNAseq (**Figure 4B, Figure S4A**). STB-associated cells comprised only 1.92% of the scRNAseq dataset compared to 15.3% of the snRNAseq dataset, underscoring the enhanced detection of this multinucleated population by nuclear profiling (**Figure 4B**). UMAP projection of the combined dataset identified eight trophoblast clusters, including two proliferating CTB (CTBp) clusters, five non-proliferating CTB clusters, and one STB cluster, defined based on canonical subtype markers (**Figure S4B**). Proliferative CTBs were overrepresented in s-RNAseq, accounting for 41.6% of cells versus 27.3% in snRNAseq. Despite these modality-specific biases, non-proliferating CTBs remained the dominant population in both datasets, representing 56.5% and 57.4% of cells in sc-RNAseq and snRNAseq, respectively (**Figure 4B**).

Given the improved detection of the STB by snRNAseq, we focused our subsequent analysis on the snRNAseq dataset, as our prior work demonstrated that this sequencing modality more effectively resolves STB heterogeneity in hTOs[12]. We sought to determine whether a similar degree of complexity was present in rTOs. After quality control filtering, 20,177 rTO nuclei were

313 retained for analysis. Clustering revealed seven distinct trophoblast populations: CTBp clusters,
314 one non-proliferative CTB cluster, one invasive CTB (iCTB) cluster, and three STB clusters
315 (**Figure 4C**, **4D, S4C**). These clusters expressed canonical markers of distinct trophoblasts,
316 including markers of proliferation (e.g., *MKI67*, *CCNA2*), CTBs (e.g., *CDH1*, *KRT7*), invasive
317 CTBs (e.g., *ITGA6*, *NOTCH2*), and STB (e.g., *HOPX*, *CGA*, *ENSMMUG00000039210*) (**Figure**
318 **4E**). Cluster-specific expression patterns were also evident. For example, *COL15A1*, *LAMB4*, and
319 *PTGER3* marked the iCTB cluster; *TAFA2*, and *TIMP3* were enriched in CTBp-1; while *HOPX*,
320 *FYN*, and *ENSMMUG00000057397* were selectively expressed in various STB clusters (**Figure**
321 **S4D**). These data highlight the transcriptional heterogeneity of rTO trophoblasts and support the
322 presence of discrete subpopulations within the STB lineage.

323 To further investigate the differences among STB subtypes, we examined the expression
324 of the RM *CGB* and *PSG* genes identified above. These genes were selectively expressed in the
325 STB-2 and STB-3 clusters, suggesting that these populations represent more differentiated STB
326 states (**Figure 4F**). In contrast, the STB-1 cluster exhibited high expression of *ERVFRD-1*, an
327 endogenous retroviral gene known to mediate trophoblast cell fusion (**Figure 4E**). This pattern
328 suggests that STB-1 may represent an immature STB cluster and/or a transitional state
329 undergoing fusion from CTB to STB. To dissect transcriptional differences among STB
330 subpopulations, we examined the top differentially expressed genes (DEGs) in each STB cluster.
331 STB-2 and STB-3 showed strong expression of rhesus *CGBs* (*ENSMMUG00000040968*,
332 *ENSMMUG00000063643*, *ENSMMUG00000049714*) and *PSGs* (*ENSMMUG00000039210*,
333 *ENSMMUG00000050799*, *ENSMMUG00000047533*) (**Figure 4G**). In contrast, STB-1 lacked
334 these markers and instead expressed *MED12L*, *DIAPH3*, and *CENPP*, genes associated with
335 transcriptional regulation, cytoskeletal remodeling, and cell division. These features suggest that
336 STB-1 represents an immature or transitional syncytial state. STB-3 was distinguished by
337 expression of several uncharacterized macaque-specific transcripts (*e.g.*,

338 *ENSMMUG00000039366*, *ENSMMUG00000039391*), highlighting potential species-specific
339 features of terminal STB differentiation.

340 To define functional differences among STB subtypes, we performed GO enrichment
341 analysis on cluster-specific differentially expressed genes. This analysis revealed distinct
342 biological programs associated with each subtype (**Figure 4H**). STB-1 was strongly enriched for
343 cell cycle–related pathways, including chromosome segregation, DNA replication, and mitotic cell
344 cycle phase transition (e.g., *CENPP*, *CCNE1*, *WEE1*, *CHEK2*), consistent with a proliferative or
345 fusion-competent syncytial precursor population. STB-2 was enriched for processes related to
346 vesicle trafficking, including post-Golgi vesicle-mediated transport. Representative genes
347 included *SEC22B*, *RAB27A*, *TMED10*, and *WLS*, indicating specialization in regulated secretion,
348 possibly of hormones or signaling molecules. STB-3 was enriched for pregnancy- and immune-
349 regulatory pathways such as Fc receptor–mediated stimulatory signaling, regulation of leukocyte
350 activation, response to estradiol, placenta development, positive regulation of cell secretion, and
351 in utero embryonic development (**Figure 4H**). The top 20 genes associated with two of these
352 pathways, positive regulation of cell secretion and Fc receptor mediated stimulatory signaling
353 pathway, show an enrichment of these genes specifically in STB-3 (**Figure 4I**, **4J**). Together, these
354 enrichment results support a model in which STB-1 represents a cycling or fusion-ready precursor
355 population, STB-2 is specialized for vesicular sorting, and STB-3 carries out immune-modulatory
356 and pregnancy-associated functions. This functional stratification underscores the transcriptional
357 and biological heterogeneity of the STB within rTOs.

358

359 **Pseudotime Analysis Identifies Distinct Stages of STB Differentiation and Function in**
360 **rTOs**

361 To compare the progression of STB differentiation in rTOs and hTOs, we performed trajectory
362 analysis using previously published hTO datasets[12] alongside rTO data. Pseudotime analysis is
363 a powerful approach for modeling gene expression dynamics along differentiation lineages and

364 identifying regulatory genes and pathways that drive cell state transitions. We applied the
365 Slingshot algorithm to infer pseudotime trajectories from sc- and sn-RNA-seq datasets, enabling
366 reconstruction of the CTB to STB differentiation continuum in both species. Global lineage
367 structures were inferred without predefining root or terminal clusters, allowing unbiased trajectory
368 detection across trophoblast states. We visualized the resulting pseudotime trajectories on UMAP
369 embeddings of rTO and hTO datasets derived from snRNAseq (**Figure 5A–B, S4E**) and
370 scRNAseq (**Figure S5A–B**). In both modalities, we identified a continuous developmental
371 trajectory originating from proliferative CTBs (CTB-p), passing through non-proliferative CTBs,
372 and culminating in the STB cluster (**Figures 5A, 5B; S5A, S5B, S5C, S5E; Table S8-9**). In rTOs,
373 the inferred lineage structure revealed two distinct branches emerging from the CTB
374 compartment: one progressing from STB-1 directly to STB-3, and a second, independent branch
375 terminating in STB-2 (**Figure 5A, Figure S4E**). This suggests that STB-2 may represent a distinct
376 differentiation pathway or functional state, rather than a transitional intermediate. To further define
377 gene expression dynamics along these trajectories, we used tradeSeq to model pseudotime-
378 dependent expression changes in both rTOs and hTOs. In rTOs, canonical STB markers such as
379 *GCM1* and *MAN1A2* increased along the STB-1 to STB-3 trajectory (**Figure 5C**), while expression
380 of CTB markers including *CDH1* declined **(*Figure 5G, S5G*).** *ERVFRD-1*, an endogenous
381 retroviral fusion gene associated with trophoblast syncytialization, was also upregulated along
382 this path (**Figure 5G**). In hTOs, a similar increase in STB markers (e.g., *CYP11A1*, *PSG5*, and
383 *HOPX)* was observed along the pseudotime axis (**Figures 5D, 5F, S5D, S5F, Table S10-11**),
384 accompanied by a loss of *CDH1* expression and an increase in *PSG9* (**Figure 5H, S5H**). Together,
385 these data define conserved and divergent gene expression dynamics underlying CTB-to-STB
386 differentiation in human and rhesus TOs. The presence of branching trajectories in rTOs suggests
387 subtype-specific regulatory programs and highlights the power of pseudotime analysis to resolve
388 complex lineage relationships during STB development.
389

390 **Pseudotime analysis uncovers species-specific gene trajectories in the STB lineage**
391 **between rTOs and hTOs**

392 Given the significant differences in gene expression profile of STB cells between rTOs and hTOs,
393 we conducted a comparative Slingshot pseudotime trajectory analysis using the integrated rTO
394 and hTO scRNAseq dataset to infer gene expression along the CTBp to STB differentiation. This
395 pseudotime analysis revealed a continuous STB trajectory, progressing from proliferative CTB to
396 non-proliferating CTB and finally to the differentiated STB subtype (**Figure S6A**). STB
397 differentiation was characterized by increased expression of well-known STB markers *INSL4*,
398 *PDLIM2*, *HMOX1*, *GCN1*, and *ERVFRD-1*, which were upregulated in both rTOs and hTOs
399 **(Figure S6B, S6C, S6D, Table S12)**. Next, we compared species-specific gene trajectories
400 between rTOs and hTOs by analyzing the integrated dataset, separating the data by condition.
401 This analysis revealed species-associated differences in gene expression along the STB
402 trajectory in rTOs and hTOs. The rTO gene trajectory showed increased expression of *PAGE4*,
403 *SLC2A1*, *WNT5A*, and *NGF* in the STB trajectory, while these genes were unchanged or
404 downregulated in the hTO trajectory (**Figure S6E-S6H**). Conversely, *SDC3*, *TGFB1*, *HSPB1*, and
405 *ESAM* specifically increased only in the hTO STB trajectory, with no similar increase in rTOs
406 (**Figure S6I-S6L**). Altogether, these findings highlight species-specific differences in gene
407 expression dynamics along the STB differentiation trajectory.

408

409 **Transcriptional Profiling of EVT Differentiation in Rhesus Trophoblast Organoids**

410 In rTO scRNAseq and snRNAseq datasets, a distinct EVT cluster was not detected, consistent
411 with prior findings in hTOs under basal culture conditions[12]. To determine whether EVT
412 differentiation could be induced in rTOs, protocols previously developed for hTOs[11,13,22] were
413 adapted and tested in the rhesus system. This multi-step differentiation process, which includes
414 treatment with Neuregulin-1 (NRG1), has been shown to promote EVT fate in human trophoblast
415 organoids[11,13,22]. Following induction, snRNAseq was performed on three independent rTO lines

416 to evaluate the extent of EVT differentiation and associated transcriptional changes. To assess
417 whether EVT differentiation was successfully induced, snRNAseq data from control (mock-
418 treated) and EVT-differentiated (EVT^{enrich}) rTOs were integrated for comparative analysis. The
419 combined dataset revealed eight transcriptionally distinct clusters, including two proliferative CTB
420 clusters (CTBp), three non-proliferative CTB clusters, one STB cluster, and one prominent EVT
421 cluster based on canonical gene expression (**Figure 6A-6C**). Most CTBp and CTB populations
422 were present at comparable frequencies between conditions. For example, CTBp-1 accounted
423 for 27.8% of nuclei in EVT^{enrich} rTOs and 28.7% in controls, while CTBp-2 and CTBp-3 remained
424 under 6% in both conditions (**Figure 6B**). Similarly, CTB-1 and CTB-2 were detected at roughly
425 10–13% in both groups. The primary difference within the CTB compartment was CTB-3, which
426 was more abundant in mock-treated rTOs (24.4%) compared to EVT^{enrich} samples (17.0%)
427 (**Figure 6B**). A marked expansion of the EVT cluster was observed in the EVT^{enrich} condition,
428 where EVT cells made up 21.5% of total nuclei, compared to just 4.33% in mock-treated rTOs
429 (**Figure 6A**, **6B**). In contrast, the STB cluster was reduced following EVT differentiation,
430 comprising 2.87% of nuclei in EVT^{enrich} rTOs compared to 13.5% in mock-treated controls, similar
431 to previous findings in hTOs, where STB representation similarly declined under EVT-inducing
432 conditions[12]. The EVT cluster was defined by expression of canonical rhesus EVT markers
433 previously described *in vivo*[14], including *TIMP2*, *NOTCH2*, *GRHL1*, and *NCAM1* (**Figure 6C**).
434 While *MAMU-AG*, a rhesus-specific homolog of *HLA-G*, is a well-established EVT marker, it was
435 not detected in our dataset, likely due to limitations in transcript annotation or insufficient read
436 coverage in this region.

437 To more fully characterize trophoblast heterogeneity and differentiation trajectories under
438 EVT-inducing conditions, snRNAseq data from the EVT^{enrich} rTOs were re-analyzed
439 independently. UMAP projection of this subset revealed eight distinct clusters: two proliferative
440 cytotrophoblast clusters (CTBp-1 and CTBp-2), one non-proliferative CTB cluster, a pre-fusion
441 CTB population marked by high expression of endogenous retroviral transcripts (CTBpf), two EVT

clusters (EVT-1 and EVT-2), one transitioning trophoblast population (TB-t), and a single STB cluster (**Figure 6D**). Quantification of cluster representation revealed that EVT-1 and EVT-2 together accounted for over 50% of all nuclei in the EVT^{enrich} rTO condition (**Figure 6E**), indicating successful and efficient induction of EVT differentiation across multiple rTO lines. The pre-fusion CTB cluster exhibited high expression of ERVFRD-1, consistent with a fusion-competent intermediate (**Figure 6F**). The TB-t cluster displayed intermediate expression of both CTB and EVT-associated genes, suggesting a transitional state along the EVT differentiation trajectory. Canonical marker analysis confirmed the identity of each population. Both EVT-1 and EVT-2 clusters expressed established rhesus EVT markers, including *TIMP2*, *GRHL1*, *NOTCH2*, and *NCAM1* (**Figure 6F**). *NOTCH2* and *NCAM1* were more highly expressed in EVT-1, suggesting that it represents a more mature EVT state.

To further resolve heterogeneity within the EVT lineage, differentially expressed genes were analyzed between EVT-1 and EVT-2. EVT-1 was enriched for genes associated with extracellular matrix remodeling, cell adhesion, and migration, such as *ITGA1*, *COL15A1*, *PTK2B*, and *PROM1*, suggesting a more invasive and mature phenotype (**Figure 6G**). In contrast, EVT-2 expressed higher levels of genes involved in signaling, cell polarity, and epithelial organization, including *NPAS3*, *LRP2*, *EFNA5*, and *TIMP3* (**Figure 6G**). These patterns indicate that EVT-1 and EVT-2 may represent distinct functional states or maturation stages within the EVT lineage. To determine if these transcriptional differences reflected a progression in differentiation, trajectory analysis was performed using Slingshot. The inferred lineage trajectory followed a path from CTBp-1 → EVT-2 → CTB → EVT-1, consistent with a model in which EVT-2 represents an earlier transitional state and EVT-1 a more terminal, differentiated population (**Figure 6H**). To test this, cells in the top 10% of pseudotime values along this lineage were isolated as a proxy for the most mature EVT state (**Figure 6I**). This subset was highly enriched for canonical markers of mature EVT identity, including *PCSK5*, *TEAD1*, *ELMO1*, *PPARG*, and *WIPF1* (Figure 6J). These results

support a model in which EVT-1 corresponds to a terminal, functionally specialized state characterized by matrix remodeling and migratory potential, while EVT-2 reflects an earlier or less differentiated phase of EVT development.

EVT Populations Are Transcriptionally Distinct Between Rhesus and Human TOs

To investigate species-specific features of EVT differentiation, we integrated snRNAseq datasets from EVT^{enrich} rTOs (rEVT) with a previously published dataset of EVT^{enrich} hTOs (hEVT) [12]. This analysis revealed eight transcriptionally distinct clusters (**Figure 7A**), with both shared and species-enriched populations. Several clusters showed a balanced representation from both species, indicating conserved transcriptional programs. CTB-1 and CTB-2 contained near-equal proportions of hEVT and rEVT cells (CTB-1: 52% hEVT / 48% rEVT; CTB-2: 57% hEVT / 43% rEVT) (**Figure 7B, S8B**). CTBp was enriched in rEVT (72%) but still contributed a substantial fraction of cells from hEVT (28%), consistent with a shared progenitor state that may differ in expansion or persistence across species. In contrast, other clusters exhibited striking species-specific enrichment. EVT-1, the dominant EVT population, was heavily skewed toward rhesus cells (69% rEVT / 31% hEVT), while EVT-2 was strongly human-enriched (95% hEVT / 5% rEVT), suggesting divergent EVT maturation pathways or regulatory programs. The STB cluster also showed species bias, with 72% of cells from hEVT and 28% from rEVT, though earlier analyses demonstrated overall conservation of STB transcriptional identity between species. Finally, CTB-4, a minor cluster, was almost exclusively derived from rEVT (93% rEVT / 7% hEVT), raising the possibility of a rhesus-specific trophoblast population or transitional state. Together, these data highlight both conserved and divergent features of trophoblast differentiation in human and rhesus organoids. While core CTB populations are largely shared, EVT subtypes show pronounced species-specific enrichment, underscoring evolutionary divergence in EVT development.

Analysis of cluster markers confirmed expression of canonical genes defining each trophoblast population, including CTBp markers (*MKI67*, *CCNA2*, *PCNA*), CTB markers (*CDH1*,

494 *CLDN4*, *EPCAM*), EVT markers (*NOTCH2*, *GRHL1*, *NCAM1*, *HLA-G*, *DIO2*, *CXCR6*), and STB
495 markers (*HOPX*, *INSL4*, *SDC1*) (**Figure 7C**). To compare EVT differentiation across species, we
496 examined expression of EVT markers in EVT^{enrich} rTOs and hTOs. Only 6.4% of EVT markers
497 were shared between species (**Figure 7D**), highlighting substantial divergence in EVT identity. To
498 explore these species-specific differences, we analyzed both shared and cluster-specific markers
499 within the EVT populations (**Figure 7E**). Shared markers included *ITGA1* and *SMAD3*, consistent
500 with conserved roles in adhesion and TGF-β signaling. In contrast, *SLC43A1* and *SEPTIN5* were
501 enriched specifically in EVT-1, while *HSPG2* and *FN1* were selectively expressed in EVT-2,
502 reflecting distinct regulatory programs within each cluster. Pseudotime analysis of the integrated
503 EVT^{enrich} rTO and hTO datasets revealed lineage trajectories to both EVT clusters (**Figure 7F**).
504 Each trajectory originated in CTBp populations, progressed through intermediate CTB states, and
505 terminated in its respective EVT cluster (**Figure 7G**), supporting the presence of structured
506 differentiation routes in both species. To assess species-specific differences in EVT gene
507 expression, we next subsetted EVT cells from the integrated dataset and performed differential
508 expression analysis between rhesus and human EVTs (**Figure 7H**). In rhesus EVTs, *ITGB8* and
509 *HTRA1* were significantly enriched, while human EVTs showed increased expression of *ANXA2*
510 and *FN1*. Gene ontology enrichment analysis of these species-specific genes revealed distinct
511 pathway associations, including the upregulation of small GTPase-mediated signal transduction
512 in human EVTs and the upregulation of DNA conformation change in rhesus EVTs (**Figure 7I, 7J**).
513 Together, these results underscore the molecular divergence between rhesus and human EVTs,
514 despite shared lineage structure and induction conditions.
515

516 **Discussion**

517 Existing *in vitro* models have failed to capture the cellular and transcriptional complexity
518 of the rhesus macaque placenta. In this study, we established and comprehensively characterized
519 rhesus trophoblast organoids using immunostaining, bulk RNA sequencing, and both single-cell

520 and single-nucleus RNA sequencing, generating a detailed transcriptional map of primate
521 trophoblast differentiation. We demonstrate that rTOs recapitulate key transcriptional signatures
522 and secretory functions of the *in vivo* rhesus placenta. High-resolution single-cell and single-nuclei
523 analyses revealed that rTOs give rise to distinct trophoblast lineages, enabling the identification
524 of specific markers for rhesus CTBs, STB, and EVTs. This platform supports direct cross-species
525 comparisons, and integration with human trophoblast organoid datasets revealed conserved STB
526 transcriptional programs but divergent EVT identities. Pseudotime trajectory analysis further
527 uncovered species-specific differentiation pathways along both the STB and EVT lineages.
528 Collectively, these findings establish rTOs as a tractable model for studying primate-specific
529 features of placentation and provide a valuable resource for investigating trophoblast biology
530 across evolution.

531 Comparative analyses of select *in vitro* models of human trophoblasts and primary
532 placental tissue have highlighted key limitations in their ability to fully recapitulate *in vivo* biology[23].
533 For example, while monolayer cell lines (e.g. BeWo, JEG-3, and JAR) are easy to culture, they
534 are tumor-derived and do not spontaneously differentiate into multiple trophoblast lineages. While
535 primary human trophoblasts do differentiate (e.g., to form fused STB), they have limited
536 proliferation capability and a short life span in cell culture. TSC models overcome many of these
537 limitations but have limited ability to differentiate into all trophoblast lineages and require
538 exogenous agents for proliferative trophoblasts to differentiate into specific trophoblast
539 populations, particularly when grown in two-dimensions. Previously described human trophoblast
540 and decidua organoids have provided a physiologically relevant model of the maternal-fetal
541 interface that is able to spontaneously differentiate into distinct trophoblast lineages and
542 recapitulate the transcriptional profile of placental tissue across gestation[9,11,15]. Of note, hTOs
543 derived from late gestation placental tissue more closely recapitulate the transcriptional signature
544 of the first trimester placenta[11,12]. It remains uncertain whether the rTOs described here accurately
545 replicate the rhesus macaque placenta during the first trimester. However, mCG secretion in

546 macaques occurs only during the early stages of pregnancy and is undetectable after day 40,
547 suggesting that rTOs most likely resemble the first trimester placenta, as we observed mCG
548 secretion. Studies comparing rTOs to first trimester placental tissue are limited by the inherent
549 challenges of accessing early gestation samples from nonhuman primates. Due to ethical and
550 logistical constraints, such tissue is rarely available, and as a result, we utilized placental samples
551 from rhesus macaques that had previously undergone experimental treatment. While these
552 conditions were not designed specifically for placental studies, we derived multiple independent
553 rTO lines from different animals and observed no consistent differences in organoid formation,
554 lineage composition, or transcriptional profiles across lines. Our use of available tissue reflects
555 the broader difficulty of conducting early pregnancy research in nonhuman primates and
556 underscores the importance of optimizing and validating *in vitro* models like rTOs to extend the
557 utility of these rare samples.

558 In both rhesus macaque and human placentas, the STB plays a critical role in nutrient
559 exchange, hormone production, and immune protection by forming the outermost cell layer of the
560 placenta that interfaces with maternal blood. While the overall function of the STB is conserved
561 across both species, there are differences in structure and cellular dynamics. In humans, the
562 STB is characterized by an extensive, highly vascularized surface area with numerous microvilli
563 and a uniform, thin multinucleated layer, optimizing nutrient and gas exchange. In contrast, the
564 rhesus macaque STB has a slightly less extensive surface area with a change in phenotype that
565 occurs after implantation has begun[24]. These differences reflect species-specific adaptations in
566 placental structure and function. Our findings demonstrate both similarities and differences in the
567 gene expression profiles of the STB between rhesus macaques and humans. We observed the
568 expression of canonical markers of the STB, including *HOPX* and *CGA*, in both rhesus macaque-
569 and human-derived organoids. These markers, known for their roles in trophoblast function and
570 placental development, were consistently present across both species, underscoring the
571 conserved nature of STB gene expression across species. Despite conservation of select

572 canonical markers, we also identified divergence in the transcriptional profiles of the STB between
573 rhesus macaque and humans. For example, while *PAGE4* is a known CTB marker in the human
574 placenta, its expression increased along the STB trajectory in rTOs[25]. Additionally, genes such as
575 *WNT5A* and *NGF*, which are involved in STB differentiation in rhesus macaques, were not
576 observed in humans. These genes have been shown to be upregulated in the rhesus macaque
577 placenta compared to the human placenta[4]. These findings highlight the complex interplay
578 between conserved functions and species-specific adaptations in the STB, which might provide
579 valuable insights into the evolutionary pressures shaping placental biology and offering new
580 models for further comparative studies.

581 Placental genes and signaling pathways are conserved along primates, but differences in
582 gene expression have been observed associated with placental development[4]. While the
583 placentas of rhesus macaques and humans are both hemochorial and discoid, there are
584 differences in their development and structure. A key difference is the trophoblast invasion in the
585 rhesus macaque placenta compared to the human placenta. EVT invasion is crucial for anchoring
586 the placenta to the uterine wall and remodeling maternal blood vessels to ensure adequate blood
587 supply to the fetus in both rhesus macaque and human placentas. However, in humans, EVT
588 invasion is more extensive, penetrating deep into the decidua and myometrium, whereas in
589 rhesus macaques, the invasion is restricted and localized, reflecting species-specific adaptations
590 in placental structure and function[24,26]. These structural differences in EVTs may stem from distinct
591 gene expression profiles and signaling cues between rhesus macaque and human trophoblasts.

592 There has been no true consensus on confirmed EVT markers in the rhesus macaque
593 placenta. Previous studies have shown that many human-associated EVT markers are present in
594 STB cells in rhesus macaques, complicating the identification of true EVT markers in this
595 species[14]. These findings underscore the species-specific differences in gene expression and
596 cellular identity between rhesus macaque and human placentas. In this study, we validated
597 *NCAM1*, *GRHL1*, and *NOTCH2* as robust EVT markers in rTOs, demonstrating that organoid

models enable precise characterization of trophoblast subtypes in nonhuman primates. By leveraging these models, we identified reliable lineage markers and observed significant divergence in EVT transcriptional programs between rTOs and hTOs. While we identified strong conservation of STB identity across species, our results highlight the distinct nature of EVT differentiation pathways. By directly comparing EVT cells in rTOs and hTOs using differential expression, we observed increased expression of *ITGB8* and *HTRA1* in rhesus macaques and *ITGA5* and *FN1* in humans. The genes associated with the regulation of small GTPase mediated signal transduction pathway are also upregulated in human EVT cells and this pathway is known to play a role in EVT migration and invasion[27]. Upregulated genes in rhesus macaque EVTs were associated with the DNA geometric change pathway. Genes associated with this pathway include *HMGB1*, *HMGB3*, and *CH1D* pertinent for transcriptional changes required for EVT properties. These species-specific differences in GO enrichment for upregulated genes are consistent with the known differences in EVTs between rhesus macaques and humans. Organoid systems thus provide a critical platform for cross-species comparisons of specific trophoblast cell types, offering new insights into both conserved and divergent features of primate placental development. More broadly, these findings reflect evolutionary adaptations in trophoblast function that align with species-specific reproductive strategies and support the use of species-matched organoid models to uncover the unique regulatory mechanisms shaping placental biology.

The studies presented here establish rhesus trophoblast organoids as a tractable *in vitro* model for detailed transcriptional profiling of placental cell types. Our findings reveal cell type–specific differences between rhesus macaque and human trophoblasts, providing new insights into species-specific aspects of placental biology. The ability to directly compare human and rhesus trophoblast organoids offers a powerful platform to investigate the evolutionary adaptations that have shaped primate placentation. Leveraging these models enables dissection of both conserved and divergent mechanisms underlying placental development and function, offering a unique window into the evolution of reproductive strategies across species.

Acknowledgements

This work was supported by the NIH grant AI145828 (C.B.C.), P01AI129859 (A.K. and C.B.C.), and the Tulane National Primate Research Center (TNPRC) NIH Base Grant P51OD011104; RRID: SCR_008167. We also gratefully acknowledge the Duke Light Microscopy Core Facility, Duke Center for Genomic and Computational Biology (GCB), Duke Proteomics and Metabolomics Core, the University of Wisconsin National Primate Research Center, and the Veterinary Medicine staff at TNPRC.

650 **Supplemental Table 1. Metadata of animal study design.**

Tissue Code	
01	CMV-seropositive healthy pregnancy; CD8b depleted at 55 days gestation, ~141 days gestation age- elective C-section
02	CMV-seronegative dams inoculated with FL-RhCMV + RhCMV UCD52 in early 2nd trimester and C-section near term gestation
03	
04	
05	
06	
07	CMV-seropositive healthy pregnancy; Anti-CD20 antibody administered for B Lymphocyte depletion at 53 days gestation and elective C-section at 144 days gestation

651

652

653

654

655

656

657

658

659

660

661

662

663

664

665

666 **Supplemental Table 2.** Metadata of trophoblast organoid lines.

Experiment	TO code	Gestational age	TOs sex	TO passage number
Bulk RNA-seq of rTOs	rTO02	154d	F	P3
	rCO02	154d	F	P3
	rCO01	141d	F	P2
Bulk RNA-seq of rDOs	rDO01	141d	F	P5
	rDO02	154d	F	P2
Bulk RNA-seq of hTOs	TO74	41w	M	P5
	CO80	40w	F	P3
	CO82	40w	M	P3
Bulk RNA-seq of hDOs	DO77	40w	F	P4
	DO76	40w	F	P5
Mass Spectrometry	rCO02	154d	F	P3, P4, P7
	rCO05	143d	F	P3, P6, P7
Radioimmunoassay	rTO02	154d	F	P3, P5, P6, P7
	rTO05	143d	F	P6, P7
	rTO04	149d	F	P4
scRNAseq of rTOs	rCO01	141d	F	P3
	rCO02	154d	F	P2
	rTO02	154d	F	P4
	rTO05	143d	F	P3
scRNAseq of hTOs	CO80	40w	F	P5
	TO68	27w	M	P12
	CO82	40w	M	P4
	CO81	40w	F	P4
snRNAseq of rTOs	rCO01	141d	F	P5
	rCO02	154d	F	P12
	rTO05	143d	F	P4
snRNAseq of EVT-differentiated rTOs	rCO01	141d	F	P2
	rCO02	154d	F	P3
	rTO05	143d	F	P7

667
668
669
670

Supplemental Table 3. Components of term trophoblast organoid (tTOM) media.

Media Components	Final Concentration
100X N2	1X
50X B27	1X
500X Primocin	100ug/mL
80X N-Acetyl-L-cysteine (NAC)	1.25mM
100X L-glutamine	2mM
10000X A83-01	500nM
10000X CHIR99021	1.5μM
2000X Recombinant human EGF	50ng/mL
2000X Recombinant human R-spondin1	80ng/mL
2000X Recombinant human FGF2	100ng/mL
2000X Recombinant human HGF	50ng/mL
100X Nicotinamide	10mM
200X Y-27632	5μM
2000X PGE2	2.5μM
FBS	10% (vol/vol)
Advanced DMEM/F12	1X

.

Supplemental Table 4. Components of decidua organoid media

Media Components	Final Concentration
100X N2	1X
50X B27	1X
500X Primocin	100ug/mL
80X N-Acetyl-L-cysteine (NAC)	1.25mM
100X L-glutamine	2mM
10000X A83-01	500nM
2000X Recombinant human EGF	50ng/mL
2000X Recombinant human R-spondin1	80ng/mL
2000X Recombinant human FGF10	100ng/mL
2000X Recombinant human HGF	50ng/mL
1000X Recombinant human Noggin	100 ng/mL
100X Nicotinamide	10mM
Advanced DMEM/F12	1X

Supplemental Table 5. Components of EVT differentiation media 1.

Media Components	Final Concentration
2-Mercaptoethanol	0.1mM
Neuregulin 1 (NRG1)	100ng/mL
Penicillin/Streptomycin	0.5% (vol/vol)
100X L-glutamine	2mM
10000X A83-01	7.5μM
Knockout Serum Replacement	4% (vol/vol)
200X Y-27632	2.5μM
ITS-X supplement	1% (vol/vol)
BSA	0.3% (vol/vol)
Advanced DMEM/F12	1X

Supplemental 6. Components of EVT differentiation media 2.

Media Components	Final Concentration
2-Mercaptoethanol	0.1mM
Penicillin/Streptomycin	0.5% (vol/vol)
100X L-glutamine	2mM
10000X A83-01	7.5μM
Knockout Serum Replacement	4% (vol/vol)
200X Y-27632	2.5μM
ITS-X supplement	1% (vol/vol)
BSA	0.3% (vol/vol)
Advanced DMEM/F12	1X

870 **Supplemental Table 7.** Antibodies used for immunofluorescence staining.

Antibody	Source	Catalog number	Additional Information
Mouse monoclonal Cytokeratin-19	Abcam	ab9221	1:500
Rabbit monoclonal Cytokeratin-19	Abcam	ab52625	1:500
Mouse monoclonal Mucin 5AC	Abcam	ab3649	1:500
Rabbit polyclonal E-cadherin	Invitrogen	PA5-85088	1:500
Rabbit monoclonal SDC-1	Abcam	ab128936	1:500
ITGA6			
Alexa Fluor 594-conjugated phalloidin	Invitrogen	A12381	1:1000
Alexa Fluor 488 Goat Anti-mouse IgG secondary antibody	Invitrogen	A32723	Secondary antibody 1:1000
Alexa Fluor 594 Goat Anti-mouse IgG secondary antibody	Invitrogen	A11032	Secondary antibody 1:1000
Alexa Fluor 594 Goat Anti-rabbit IgG secondary antibody	Invitrogen	A11037	Secondary antibody 1:1000

871
872
873
874
875
876
877
878
879
880
881
882
883
884
885

886 **Materials and Methods**

887 **Rhesus macaque samples.** Placental tissues were obtained at Caesarian section from seven
888 third trimester pregnant Indian-ancestory rhesus macaques housed at the Tulane National
889 Primate Research Center (TNPRC). The pregnant females included five rhesus cytomegalovirus
890 (RhCMV)- seronegative dams experimentally infected with two RhCMV strains in early second
891 trimester gestation, and two RhCMV-seropositive dams that were experimentally depleted of
892 either CD8+ T-lymphocytes or CD20+ B-lymphocytes in late first trimester gestation. All animals
893 remained healthy until the time of elective Caesarian section conducted between 141-154
894 gestation days. All macaques were from the specific pathogen free breeding colony at TNPRC
895 and free of SIV, STLV, Type D retrovirus and herpes B virus. The study was approved by the
896 TNPRC Institutional Animal Care and Use Committee (IACUC) and conducted in accordance with
897 the Guide for the Care and Use of Laboratory Animals at the NIH.

898

899 **Human samples.** Human tissue used in this study was obtained from Duke University after
900 approval was received from the Duke University Institutional Review Board (IRB) and in
901 accordance with the guidelines of Duke University human tissue procurement. Human placental
902 tissue used in this study for the generation of organoids was collected from third trimester (38th-
903 41st weeks) from Caesarean sections. Tissue was collected from healthy normal donors and
904 tissue was excluded in cases of fetal anomalies or aneuploidy.

905

906 **Derivation and culture of organoids from human and rhesus macaque placental samples.**
907 Placental tissue was carefully dissected and separated into chorionic villi, smooth chorion,
908 amnion, and decidua separated. The amnion layer was kept intact and peeled from the chorion.
909 To remove decidua from the chorion, isolated chorion tissue was carefully scraped with forceps.
910 Stem/progenitor cells isolation from smooth chorion were similar to full-term chorionic villous
911 isolation previously described[11]. Briefly, dissected tissue was cut into small pieces (1-2mm^2) and

912 sequentially digested with 0.2% trypsin-250 (Alfa Aesar, J63993-09)/0.02% EDTA (Sigma-Aldrich
913 E9884-100G) and 1.0 mg/mL collagenase V (Sigma-Aldrich, C9263-100MG) on a 37°C stir plate
914 in small bottles containing stir bars. After the collagenase V digestion, tissue was disrupted
915 manually by vigorous pipetting with a 5-10mL serological pipette (10-20 times) prior to filtration.
916 Then pool two digests flow-through and pellet by centrifugation (600g for 6 minutes) and finally
917 resuspend with ice-cold growth-factor-reduced Matrigel (Corning 356231). Matrigel "domes"
918 (40ul/well) were plated into 24-well tissue culture plates (Corning 3526), placed in a 37°C
919 incubator to pre-polymerize for approximately 3 minutes, turned upside down to ensure equal
920 distribution of the isolated cells in domes for another 10 minutes, then carefully overlaid with 500
921 µL prewarmed media. For both rTOs and hTOs derivation and culture, the term trophoblast
922 organoid medium (tTOM) consisting of Advanced DMEM/F12 (Life Technologies, 12634-010)
923 supplemented with 1× B27 (Life Technologies, 17504-044), 1× N2 (Life Technologies, 17502-
924 048), 10% FBS (vol/vol, Cytiva HyClone, SH30070.03), 2 mM GlutaMAX™ supplement (Life
925 Technologies, 35050-061), 100 µg/mL Primocin (InvivoGen, ant-pm-1), 1.25 mM N-Acetyl-L-
926 cysteine (Sigma, A9165), 500 nM A83-01 (Tocris, 2939), 1.5 µM CHIR99021 (Tocris, 4423), 50
927 ng/mL recombinant human EGF (Gibco, PHG0314), 80 ng/mL recombinant human R-spondin 1
928 (R & D systems, 4645-RS-100), 100 ng/mL recombinant human FGF2 (Peprotech, 100-18C), 50
929 ng/mL recombinant human HGF (Peprotech, 100-39), 10mM nicotinamide (Sigma, N0636-100G),
930 5 µM Y-27632 (Sigma, Y0503-1MG), and 2.5 µM prostaglandin E2 (PGE2, R & D systems, 22-
931 961-0) was used. To passage, TOs were digested in prewarmed TrypLE Express (Gibco, 12605-
932 028) at 37°C for 8 min. Further mechanical dissociation was achieved by manual disruption.
933 Dissociated TOs were collected and washed by centrifuge, then resuspended in fresh ice-cold
934 Matrigel and replated as domes at the desired density for continuous culture. For freezing,
935 overlaid media was aspirated, and organoid-Matrigel domes were resuspended in CryoStor CS10
936 stem cell freezing medium (STEMCell Technologies, 07930) and frozen at -80 °C and then

937 transferred to liquid nitrogen for long-term storage. For thawing cryopreserved TOs, organoids
938 were thawed as quickly as possible, diluted with 5 times volume of basic TOM containing
939 Advanced DMEM/F12, 2 mM GlutaMAX supplement, 10 mM HEPES (Gibco, 15630-106), 1 ×
940 Penicillin/Streptomycin (Lonza, 17-602E) and centrifuged to pellet. Afterwards, TOs were
941 resuspended in new ice-cold Matrigel and replated for recovery culture and passaged as
942 described above.
943
944 **Derivation and culture of organoids from human and rhesus macaque decidua samples.**
945 Decidual tissue was dissected from human and rhesus macaque placenta and further cleaned by
946 removing as much as possible those attached chorionic villi prior to the isolation of decidua
947 glands-enriched suspension as described previously (Turco et al., 2017b; Turco et al., 2017a,
948 Yang et al., 2022). Briefly, collected decidual tissues were cut into small pieces then digested in
949 1.25 U/mL Dispase II (Sigma-Aldrich, D4693)/0.4mg/mL collagenase V (Sigma-Aldrich, C-9263).
950 Following digestion and pipetting, the decidua glandular structures were filtered out with 100 μm
951 cell strainer, then collect the glandular structures from strainer and pipette to dissociate them into
952 small pieces before resuspending with ice-cold growth-factor-reduced Matrigel (Corning 356231),
953 plated as “domes” in 24-well plates (Corning, 3526), and overlaid with 500 μL prewarmed media.
954 For decidua organoids Expansion Medium (ExM) was used with the same composition as
955 previously described[28]. ExM was renewed every 2-3 days. Mature decidua organoids were
956 passaged by mechanical disruption following TrypLE Express (ThermoFisher Scientific,
957 12605010) digestion.
958
959 **Generation of conditioned media.** Overlaid media was collected from mature organoids after 7-
960 10 days post-passaging. CM was stored at -20°C. Non-conditioned medium (NCM) was TOM

961 (described above) that had not been exposed to organoids. All experiments using CM were from
962 at least two independent TO lines.
963
964 **Hormone Secretion Assays.** Conditioned media was collected as described above and a
965 radioimmunoassay was used to quantify mCG and progesterone secretion in cell conditioned
966 media as previously described[18,19].
967
968 **Mass Spectrometry.** CM was collected from rTOs and submitted to Duke University Proteomics
969 and Metabolomics Core Facility. SDS-PAGE gel bands were subjected to in-gel tryptic digestion
970 using standardized protocols[29]. Digested peptides were lyophilized to dryness and resuspended
971 in 12 uL of 0.2% formic acid/2% acetonitrile. Each sample was subjected to chromatographic
972 separation on a Thermo Neo Vanquish UPLC equipped with a 1.7 μm HSS T3 C18 75 μm I.D. X
973 250 mm reversed-phase column (NanoFlow data). The mobile phase consisted of (A) 0.1% formic
974 acid in water and (B) 0.1% formic acid in acetonitrile. 3 μL was injected and peptides were trapped
975 for 3 min on a 5 μm Symmetry C18 180 μm I.D. X 20 mm column at 5 μl/min in 99.9% A. The
976 analytical column was then switched in-line and a linear elution gradient of 5% B to 40% B was
977 performed over 30 min at 400 nL/min. Data collection on the Fusion Lumos mass spectrometer
978 with a FAIMS Pro device was performed for three difference compensation voltages (-40v, -60v,
979 -80v). Within each CV, a data-dependent acquisition (DDA) mode of acquisition with a r=120,000
980 (@ m/z 200) full MS scan from m/z 375 - 1500 with a target AGC value of 4e5 ions was performed.
981 MS/MS scans with HCD settings of 30% were acquired in the linear ion trap in "rapid" mode with
982 a target AGC value of 1e4 and max fill time of 35 ms. The total cycle time for each CV was 0.66s,
983 with total cycle times of 2 sec between like full MS scans. A 20s dynamic exclusion was employed
984 to increase depth of coverage.

985 Raw LC-MS/MS data files were processed in Proteome Discoverer 3.0 (Thermo Scientific)
986 and then submitted to independent Sequest database searches against a Rhesus Macaque
987 protein database containing both forward (20260 entries) and reverse entries of each
988 protein. Search tolerances were 2 ppm for precursor ions and 0.8 Da for product ions using
989 trypsin specificity with up to two missed cleavages. All searched spectra were imported into
990 Scaffold (v5.3, Proteome Software) and scoring thresholds were set to achieve a peptide false
991 discovery rate of 1% using the PeptideProphet algorithm. Raw data were also imported into
992 Protein Discoverer 3.0 for area under the curve measurements of eluting peptides.
993
994 **Immunofluorescence.** Organoids were fixed in 4% PFA for 15 min at room temperature, then
995 washed in PBS. Organoids were placed in 0.25% Triton X-100/PBS to permeabilize for 15 min at
996 room temperature. Organoids were washed in 1x PBS and then incubated with the indicated
997 primary antibodies in PBS at 4°C overnight. Organoids were pelleted by gravity, washed with PBS,
998 and then incubated for 30 min at room temperature with Alexa Fluor-conjugated secondary
999 antibodies (Invitrogen). Organoids were washed again with PBS and mounted in Vectashield
1000 (Vector Laboratories) containing 4′,6-diamidino- 2-phenylindole (DAPI) and were transferred onto
1001 microscope slides with large-orifice 200 µL-tips (Fisher Scientific, 02707134). The following
1002 antibodies and reagents were used: cytokeratin-19 (Abcam, ab9221, ab52625), SDC-1 (abcam,
1003 ab128936), ITGA6 (Invitrogen, MA5-16884), E-cadherin (Invitrogen, PA5-85088), Mucin 5AC
1004 (Abcam, ab3649), Alexa Fluor 594–conjugated phalloidin (Invitrogen, A12381).
1005
1006 **Induced Differentiation of rTOs into EVT^{enrich} rTOs.** To generate EVT-enriched rTOs, we
1007 adapted established EVT differentiation protocols developed previously[11,13,22]. rTOs were
1008 passaged as described above and plated in Matrigel domes into 24-well tissue culture plates.
1009 Organoids were cultured in TOM as described above for 3-4 days, then switched to EVT

1010 differentiation media 1 [EVT m1: advanced DMEM/F12 supplemented with 2 mM L-glutamine, 0.1
1011 mM 2-mercaptoethenol, 0.5% (vol/vol) penicillin/streptomycin, 0.3% (vol/vol) BSA, 1% (vol/vol)
1012 ITS-X supplement, 100 ng/ml NRG1 (Cell Signaling, 5218SC), 7.5 μM A83-01, 2.5 μM Y27632
1013 and 4% (vol/vol) Knockout Serum Replacement (Gibco 10828010)], for 6 days. EVT m1 was
1014 renewed every 2 days for the initial 4 days then daily for the remaining culture period. Following,
1015 organoids were switched to EVT m2, which is the same recipe as described above for EVT m1
1016 but without NRG1, for a further 2-3 days, with daily media changes.
1017
1018 **RNA extraction and Bulk RNA-seq.** Total RNA was isolated with the Sigma GenElute total
1019 mammalian RNA miniprep kit or Qiagen RNAeasy Mini Kit following the manufacturer's instruction
1020 and using supplementary Sigma DNase digestion. RNA quality and concentration were
1021 determined using a Nanodrop ND-1000 Spectrophotometer. For bulk RNA-seq analysis, RNA was
1022 isolated from organoids or placenta tissue as described above. Purified Total RNA was verified by
1023 Thermo scientific Nanodrop one. The libraries were prepared by the Duke Center for Genomic
1024 and Computational Biology (GCB) using the Tru-Seq stranded total RNA prep kit (Illumina).
1025 Sequencing was performed on the NovaSeq 6000 by using 150-bp paired-end sequencing. The
1026 reads were aligned to the human or rhesus macaque reference genome (GRCh38, Mmul10) using
1027 QIAGEN CLC Genomics (v20). Differential expression analysis was performed using the DeSeq2
1028 package in R [30], k-means pathway cluster enrichment for GO Biological processes and principal
1029 component analyses (PCA) was performed using iDEP [31,32]. Heatmaps and hierarchical clustering
1030 was performed in R using the pheatmap package and were based on $\log_2$ RPKM (reads per
1031 kilobase million). Files associated with bulk RNA-seq studies have been deposited into Sequence
1032 Read Archive (PRJNA891648 and PRJNA1230745). Principal component analyses were
1033 performed using pcaExplorer in R [33]. Volcano plots were generated using the EnhancedVolcano
1034 package in R or in Graphpad Prism version 9.
1035

1036 **Dissociation of organoids for single cell and single nucleus RNA sequencing.** Organoids
1037 were dissociated by scraping Matrigel domes into 1 mL of pre-warmed TrypLE Express
1038 (Invitrogen, 12605036) and incubating at 37°C for 12 min, swirling the tube every 2-3 min.
1039 Dissociated organoids were pelleted at 1250 rpm for 3 min and re-suspended in 200 µL DMEM
1040 containing 10% FBS. Resuspended organoids were subjected to vigorous manual disruption
1041 using a single channel p200 pipette (Ranin, 17008652) for 3 min followed by the addition of 800
1042 µL of DMEM containing 10% FBS. The disrupted suspension was then passed over a 40 µm filter
1043 cell strainer (Corning, 352098). Flow through was then centrifuged at 1250 rpm for 5min and the
1044 pellet resuspended in 250 µL of 1x PBS for a final volume of ~300 µL and cell counts of ~1 x 10^6
1045 cells/mL. Cell viability was determined using trypan blue and followed by automated cell counting
1046 (Biorad TC20 automated cell counter). Sequencing was performed on three organoid lines from
1047 unique placental tissue.
1048
1049 **Single-Cell RNA-seq Library Preparation and Data Analysis.**
1050 **SC Processing**
1051 Libraries for single-cell RNA sequencing were prepared from 10k total cells using the methods
1052 described in the 10x Genomics Single Cell 3' Reagent Kit Protocol (v2 chemistry, Manual Part
1053 #CG00052). Single-cell RNA sequencing runs were performed on an Illumina NovaSeq 6000
1054 (Illumina, San Diego) using an S2 flow cell (Illumina, San Diego), which allowed for ~61k
1055 reads/cell for rTO samples. hTO sequencing was performed using an S4 flow cell (Illumina, San
1056 Diego), which allowed for ~74k reads/cell.
1057 **SN Processing**
1058 Nuclei were isolated from dissociated rTOs using 10x Genomics' Nuclei Isolation from Single Cell
1059 Suspensions protocol (10x Genomics – Pleasanton, VA). All buffers used were prepared fresh,
1060 according to manufacturer's protocol. Cell suspensions were pelleted by centrifugation at 300rcf,
1061 4°C for 5 minutes, followed by removal of the supernatant, and lysis buffer was added with gentle

1062 pipetting on ice for 5 minutes. Next, samples were washed twice with nuclei wash and
1063 resuspension buffer, followed by centrifugation at 500 rcf, 4°C for 10 minutes then supernatant
1064 removal. Nuclei are then resuspended in wash and resuspension buffer, concentatrion determend
1065 on a Cellometer Ascend Automated Cell Counter (RevvityWaltham, MA). If necessary, nulei are
1066 filtered through 40µm Flowmi Cell Strainers (Bel-Art – Wayne, NJ) to remove clumps and debris
1067 prior to proceeding with the single nuclei assay. Nuclei are visualized at 40x magnification using
1068 LifeTech EVOS FL microscope (Thermo Fisher Scientific – Waltham, MA) to determine quality via
1069 nuclear membrane intactness. Nuclei were loaded with a Chromium Reagent Kit v4. Libraries
1070 were sequenced on the Nova Seq X Plus at a targeted depth of 22,000 to 35,000 reads per
1071 nucleus.
1072
1073 **SC and SN Sequencing Data Processing**. Post-processing, quality control, and read alignment
1074 to the Mmul10 rhesus macaque reference genome or to the hg38 human reference genome were
1075 performed using 10x CellRanger package (v6.1.2, 10x Genomics). Gene expression matrices
1076 generated by the 10x CellRanger aggregate option were analyzed using Seurat (version 4.0) in
1077 R [34-37]. For SC, cells with at least 200 and no more than 10,000 unique expressed genes were
1078 included in downstream analysis, and cells with more than 10% mitochondrial reads were
1079 excluded from analysis. Dropout rate was 67-74%. For SN, nuclei with at least 200 and no more
1080 than 8,500 unique genes and less than 50,000 counts were included in downstream analysis, and
1081 nuclei with more than 1% mitochondrial reads and 5% ribosomal reads were excluded from
1082 analysis. Dropout rate was 87-89%. To eliminate batch effects, datasets from unique donors were
1083 normalized using the *sctransform* function and integrated using the *FindIntegrationAnchors()* in
1084 Seurat (version 4.0) in R [37]. Dimensional reduction was performed using the *RunPCA()* function
1085 to obtain the first 20 principal components, which was determined using *ElbowPlots()* across the
1086 first 50 dimensions. To identify clusters, Louvain clustering (Seurat *FindClusters()* function) was
1087 performed, and optimal resolution was determined using the *clustree()* function[38] on a range of

1088 resolutions between 0.2-1.0, with 0.3-0.4 used for downstream analyses. Integration of rTO and
1089 hTO datasets was performed on previously integrated datasets using the Harmony algorithm[39]
1090 (v1.0) for batch correction and alignment. Differential expression analysis between clusters was
1091 performed using the Wilcoxon rank sum test implemented in Seurat's FindAllMarkers() function.
1092 Genes with a log2 fold change > 0.25 and an FDR-adjusted p-value < 0.05 were considered
1093 significantly differentially expressed. Marker genes for each cluster were identified by searching
1094 for positively enriched genes using the aforementioned criteria. All files associated with this single
1095 cell and single nuclei RNA-seq study have been deposited into Sequence Read Archive
1096 (PRJNA1230239 and PRJNA1283913).

1097 The *slingshot* package (version 2.6.0) in R was used to determine differentiation
1098 trajectories from clusters identified in Seurat with unbiased starting and ending roots[40]. The raw
1099 counts and above-generated slingshot object were used to run *evaluateK()* with the total number
1100 of knots ranging from 3 to 9. The optimal number of knots was determined to be 4. The *fitGAM()*
1101 function using *tradeSeq* (1.5.10) was run with this resulting value and gene expression along
1102 lineages identified using the *associationTest()* function[41]. Heatmaps of expression changes
1103 across lineages were generated using *ComplexHeatmap()* on log transformed counts and
1104 rasterized using the *ImageMagick* "Bessel" filter [42]. The *plotGenePseudotime()* function was used
1105 to visualize raw count gene expression in individual cells across lineages from the *slingshot*
1106 object. Code used for data analysis and figure generation are available at CoyneLabDuke Github
1107 repository (https://github.com/CoyneLabDuke/Rhesus-Macaque-Trophoblast-Organoids).

1108

1109 **Statistics and reproducibility.** All experiments reported in this study have been reproduced
1110 using independent samples (tissues and organoids) from multiple donors. Data are presented as
1111 mean ± SD, unless otherwise stated. Statistical significance was determined as described in the
1112 figure legends. Parametric tests were applied when data were distributed normally based on
1113 D'Agostino-Pearson analyses; otherwise, nonparametric tests were applied. For all statistical

tests, p value <0.05 was considered statistically significant, with specific p values noted in the figure legends.

Literature Cited

1. Carter, A.M., and Enders, A.C. (2004). Comparative aspects of trophoblast development and placentation. Reprod Biol Endocrinol *2*, 46. 10.1186/1477-7827-2-46.
2. Carter, A.M. (2011). Comparative studies of placentation and immunology in non-human primates suggest a scenario for the evolution of deep trophoblast invasion and an explanation for human pregnancy disorders. Reproduction *141*, 391-396. 10.1530/REP-10-0530.
3. de Rijk, E.P.C.T., and Van Esch, E. (2008). The Macaque Placenta-A Mini-Review. Toxicol Pathol *36*, 108s-118s. 10.1177/0192623308326095.
4. Rosenkrantz, J.L., Gaffney, J.E., Roberts, V.H.J., Carbone, L., and Chavez, S.L. (2021). Transcriptomic analysis of primate placentas and novel rhesus trophoblast cell lines informs investigations of human placentation. BMC Biol *19*, 127. 10.1186/s12915-021-01056-7.
5. Boyson, J.E., Iwanaga, K.K., Golos, T.G., and Watkins, D.I. (1996). Identification of the rhesus monkey HLA-G ortholog. Mamu-G is a pseudogene. J Immunol *157*, 5428-5437.
6. Brinkman-Van der Linden, E.C., Hurtado-Ziola, N., Hayakawa, T., Wiggleton, L., Benirschke, K., Varki, A., and Varki, N. (2007). Human-specific expression of Siglec-6 in the placenta. Glycobiology *17*, 922-931. 10.1093/glycob/cwm065.
7. Esnault, C., Cornelis, G., Heidmann, O., and Heidmann, T. (2013). Differential evolutionary fate of an ancestral primate endogenous retrovirus envelope gene, the EnvV syncytin, captured for a function in placentation. PLoS Genet *9*, e1003400. 10.1371/journal.pgen.1003400.
8. Maston, G.A., and Ruvolo, M. (2002). Chorionic gonadotropin has a recent origin within primates and an evolutionary history of selection. Mol Biol Evol *19*, 320-335. 10.1093/oxfordjournals.molbev.a004085.
9. Turco, M.Y., Gardner, L., Kay, R.G., Hamilton, R.S., Prater, M., Hollinshead, M.S., McWhinnie, A., Esposito, L., Fernando, R., Skelton, H., et al. (2018). Trophoblast organoids as a model for maternal-fetal interactions during human placentation. Nature *564*, 263-267. 10.1038/s41586-018-0753-3.
10. Haider, S., Meinhardt, G., Saleh, L., Kunihs, V., Gamperl, M., Kaindl, U., Ellinger, A., Burkard, T.R., Fiala, C., Pollheimer, J., et al. (2018). Self-Renewing Trophoblast Organoids Recapitulate the Developmental Program of the Early Human Placenta. Stem Cell Reports *11*, 537-551. 10.1016/j.stemcr.2018.07.004.
11. Yang, L., Semmes, E.C., Ovies, C., Megli, C., Permar, S., Gilner, J.B., and Coyne, C.B. (2022). Innate immune signaling in trophoblast and decidua organoids defines differential antiviral defenses at the maternal-fetal interface. Elife *11*. 10.7554/eLife.79794.
12. Keenen, M.M., Yang, L., Liang, H., Farmer, V.J., Worota, R.E., Singh, R., Gladfelter, A.S., and Coyne, C.B. (2025). Comparative analysis of the syncytiotrophoblast in placenta tissue and trophoblast organoids using snRNA sequencing. Elife *13*. 10.7554/eLife.101170.
13. Okae, H., Toh, H., Sato, T., Hiura, H., Takahashi, S., Shirane, K., Kabayama, Y., Suyama, M., Sasaki, H., and Arima, T. (2018). Derivation of Human Trophoblast Stem Cells. Cell Stem Cell *22*, 50-63 e56. 10.1016/j.stem.2017.11.004.

14. Schmidt, J.K., Keding, L.T., Block, L.N., Wiepz, G.J., Koenig, M.R., Meyer, M.G., Dusek, B.M., Kroner, K.M., Bertogliat, M.J., Kallio, A.R., et al. (2020). Placenta-derived macaque trophoblast stem cells: differentiation to syncytiotrophoblasts and extravillous trophoblasts reveals phenotypic reprogramming. Sci Rep *10*, 19159. 10.1038/s41598-020-76313-w.
15. Keenen, M.M., Yang, L., Liang, H., Farmer, V.J., Singh, R., Gladfelter, A.S., and Coyne, C.B. (2024). Comparative analysis of the syncytiotrophoblast in placenta tissue and trophoblast organoids using snRNA sequencing. bioRxiv, 2024.2007.2001.601571. 10.1101/2024.07.01.601571.
16. Wang, M., Liu, Y., Sun, R., Liu, F., Li, J., Yan, L., Zhang, J., Xie, X., Li, D., Wang, Y., et al. (2024). Single-nucleus multi-omic profiling of human placental syncytiotrophoblasts identifies cellular trajectories during pregnancy. Nat Genet *56*, 294-305. 10.1038/s41588-023-01647-w.
17. Shimizu, K. (2008). Reproductive Hormones and the Ovarian Cycle in Macaques. Journal of Mammalian Ova Research *25*, 122-126.
18. Block, L.N., Aliota, M.T., Friedrich, T.C., Schotzko, M.L., Mean, K.D., Wiepz, G.J., Golos, T.G., and Schmidt, J.K. (2020). Embryotoxic impact of Zika virus in a rhesus macaque in vitro implantation modeldagger. Biol Reprod *102*, 806-816. 10.1093/biolre/ioz236.
19. Ziegler, T.E., Matteri, R.L., and Wegner, F.H. (1993). Detection of urinary gonadotropins in callitrichid monkeys with a sensitive immunoassay based upan a unique monoclonal antibody. Am J Primatol *31*, 181-188. 10.1002/ajp.1350310303.
20. Moore, T., Williams, J.M., Becerra-Rodriguez, M.A., Dunne, M., Kammerer, R., and Dveksler, G. (2022). Pregnancy-specific glycoproteins: evolution, expression, functions and disease associations. Reproduction *163*, R11-R23. 10.1530/REP-21-0390.
21. Matsumoto, S., Porter, C.J., Ogasawara, N., Iwatani, C., Tsuchiya, H., Seita, Y., Chang, Y.W., Okamoto, I., Saitou, M., Ema, M., et al. (2020). Establishment of macaque trophoblast stem cell lines derived from cynomolgus monkey blastocysts. Sci Rep *10*, 6827. 10.1038/s41598-020-63602-7.
22. Sheridan, M.A., Zhao, X., Fernando, R.C., Gardner, L., Perez-Garcia, V., Li, Q., Marsh, S.G.E., Hamilton, R., Moffett, A., and Turco, M.Y. (2021). Characterization of primary models of human trophoblast. Development *148*. 10.1242/dev.199749.
23. Li, X., Li, Z.H., Wang, Y.X., and Liu, T.H. (2023). A comprehensive review of human trophoblast fusion models: recent developments and challenges. Cell Death Discov *9*, 372. 10.1038/s41420-023-01670-0.
24. Carter, A.M., Enders, A.C., and Pijnenborg, R. (2015). The role of invasive trophoblast in implantation and placentation of primates. Philos Trans R Soc Lond B Biol Sci *370*, 20140070. 10.1098/rstb.2014.0070.
25. Marsh, B., Zhou, Y., Kapidzic, M., Fisher, S., and Blelloch, R. (2022). Regionally distinct trophoblast regulate barrier function and invasion in the human placenta. Elife *11*. 10.7554/eLife.78829.
26. Enders, A.C., Lantz, K.C., and Schlafke, S. (1996). Preference of invasive cytotrophoblast for maternal vessels in early implantation in the macaque. Acta Anat (Basel) *155*, 145-162. 10.1159/000147800.
27. Nicola, C., Lala, P.K., and Chakraborty, C. (2008). Prostaglandin E2-mediated migration of human trophoblast requires RAC1 and CDC42. Biol Reprod *78*, 976-982. 10.1095/biolreprod.107.065433.
28. Turco, M.Y., Gardner, L., Hughes, J., Cindrova-Davies, T., Gomez, M.J., Farrell, L., Hollinshead, M., Marsh, S.G.E., Brosens, J.J., Critchley, H.O., et al. (2017). Long-term, hormone-responsive organoid cultures of human endometrium in a chemically defined medium. Nat Cell Biol *19*, 568-577. 10.1038/ncb3516.

29. Wilm, M., Shevchenko, A., Houthaeve, T., Breit, S., Schweigerer, L., Fotsis, T., and Mann, M. (1996). Femtomole sequencing of proteins from polyacrylamide gels by nano-electrospray mass spectrometry. Nature *379*, 466-469. 10.1038/379466a0.
30. Love, M.I., Huber, W., and Anders, S. (2014). Moderated estimation of fold change and dispersion for RNA-seq data with DESeq2. Genome Biol *15*, 550. 10.1186/s13059-014-0550-8.
31. Ge, S.X., Son, E.W., and Yao, R. (2018). iDEP: an integrated web application for differential expression and pathway analysis of RNA-Seq data. BMC Bioinformatics *19*, 534. 10.1186/s12859-018-2486-6.
32. Ge, X. (2021). iDEP Web Application for RNA-Seq Data Analysis. Methods Mol Biol *2284*, 417-443. 10.1007/978-1-0716-1307-8_22.
33. Marini, F., and Binder, H. (2019). pcaExplorer: an R/Bioconductor package for interacting with RNA-seq principal components. BMC Bioinformatics *20*, 331. 10.1186/s12859-019-2879-1.
34. Hao, Y., Hao, S., Andersen-Nissen, E., Mauck, W.M., 3rd, Zheng, S., Butler, A., Lee, M.J., Wilk, A.J., Darby, C., Zager, M., et al. (2021). Integrated analysis of multimodal single-cell data. Cell *184*, 3573-3587 e3529. 10.1016/j.cell.2021.04.048.
35. Butler, A., Hoffman, P., Smibert, P., Papalexi, E., and Satija, R. (2018). Integrating single-cell transcriptomic data across different conditions, technologies, and species. Nat Biotechnol *36*, 411-420. 10.1038/nbt.4096.
36. Satija, R., Farrell, J.A., Gennert, D., Schier, A.F., and Regev, A. (2015). Spatial reconstruction of single-cell gene expression data. Nat Biotechnol *33*, 495-502. 10.1038/nbt.3192.
37. Stuart, T., Butler, A., Hoffman, P., Hafemeister, C., Papalexi, E., Mauck, W.M., 3rd, Hao, Y., Stoeckius, M., Smibert, P., and Satija, R. (2019). Comprehensive Integration of Single-Cell Data. Cell *177*, 1888-1902 e1821. 10.1016/j.cell.2019.05.031.
38. Zappia, L., and Oshlack, A. (2018). Clustering trees: a visualization for evaluating clusterings at multiple resolutions. Gigascience *7*. 10.1093/gigascience/giy083.
39. Korsunsky, I., Millard, N., Fan, J., Slowikowski, K., Zhang, F., Wei, K., Baglaenko, Y., Brenner, M., Loh, P.R., and Raychaudhuri, S. (2019). Fast, sensitive and accurate integration of single-cell data with Harmony. Nat Methods *16*, 1289-1296. 10.1038/s41592-019-0619-0.
40. Street, K., Risso, D., Fletcher, R.B., Das, D., Ngai, J., Yosef, N., Purdom, E., and Dudoit, S. (2018). Slingshot: cell lineage and pseudotime inference for single-cell transcriptomics. BMC Genomics *19*, 477. 10.1186/s12864-018-4772-0.
41. Van den Berge, K., Roux de Bezieux, H., Street, K., Saelens, W., Cannoodt, R., Saeys, Y., Dudoit, S., and Clement, L. (2020). Trajectory-based differential expression analysis for single-cell sequencing data. Nat Commun *11*, 1201. 10.1038/s41467-020-14766-3.
42. ImageMagick (2023). ImageMagick Studio LLC. . https://imagemagick.org.

1257 **Figure 1**

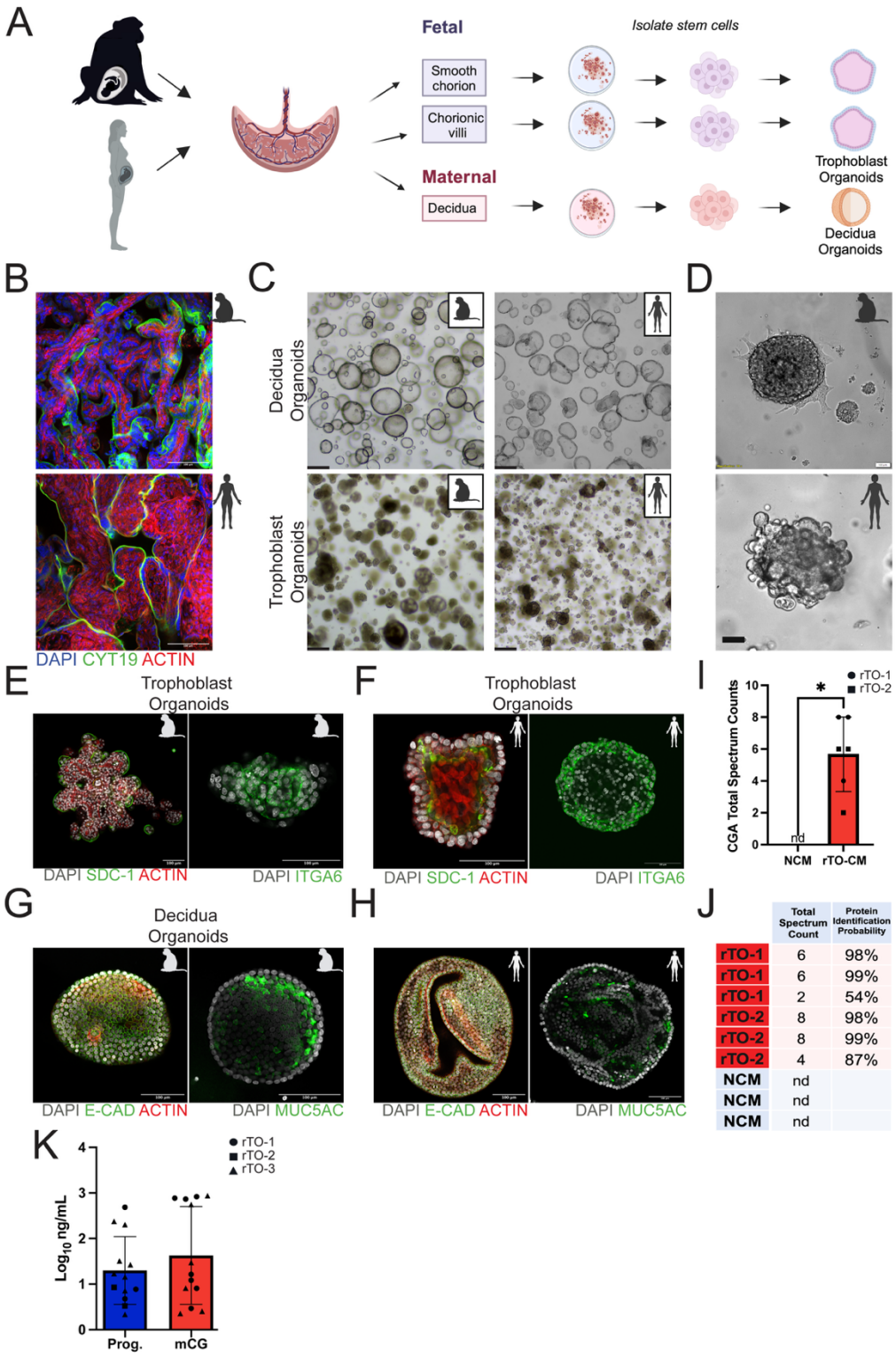

	Total Spectrum Count	Protein Identification Probability
rTO-1	6	98%
rTO-1	6	99%
rTO-1	2	54%
rTO-2	8	98%
rTO-2	8	99%
rTO-2	4	87%
NCM	nd	
NCM	nd	
NCM	nd	

1258
1259

1260 **Figure 1. Establishment and of rhesus macaque trophoblast and decidua organoids. (A),**
1261 Schematic of the rhesus macaque and human placenta denoting full-term human and mid-late
1262 third trimester rhesus macaque fetal trophoblast and maternal decidua tissues used to generate

matched organoids. Created using Biorender. **(B),** Confocal micrographs of rhesus macaque (top) and human (bottom) chorionic villi. Cytokeratin-19 is shown in green, actin is shown in red, and DAPI-stained nuclei are in blue. Scale bar, 100μm. **(C),** Top, brightfield images of representative decidua organoids of rhesus macaque (left) and human (right). Bottom, representative brightfield images of trophoblast organoids of rhesus macaque (left) and human (right) trophoblast organoids. Scale bar, 500μm **(D),** Representative brightfield images of rTOs (top) and hTOs (bottom). Scale bar, 100μm. **(E, F),** Confocal micrographs of rTOs and hTOs immunostained for SDC1 (green), ACTIN (red), DAPI-stained nuclei are in black and white on the left, ITGA6 (green), DAPI-stained nuclei are in black and white on the right. Scale bar, 100μm. **(G, H),** Confocal micrographs of rDOs and hDOs immunostained for E-cadherin (green), ACTIN (red), DAPI-stained nuclei are in black and white on the left, MUC5AC (green), DAPI-stained nuclei are in black and white on the right. Scale bar, 100μm. **(I),** Total Spectrum Counts of Chorionic Gonadotropin (CGA) in non-conditioned media (NCM) and CM isolated from two independent lines of rTOs. Each point represents an independent replicate/well. **(J),** Quantification of total spectrum count and protein identification probability of mCG. **(K),** Secretion of progesterone and mCG from three unique rTO lines measured by radioimmunoassay. Each point represents an independent replicate/well.

1313 **Figure 2**

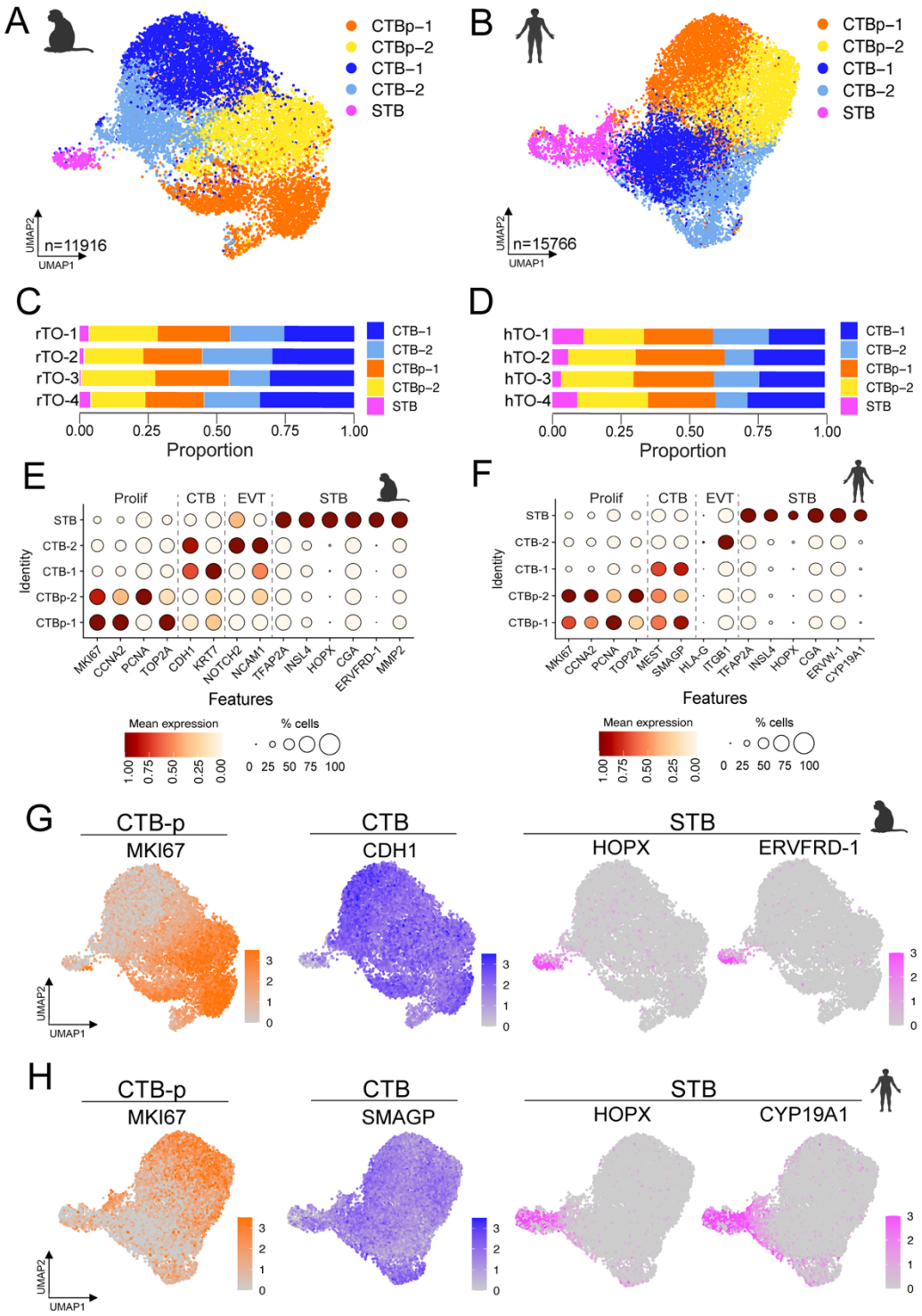

1314
1315

1316 **Figure 2. Single cell RNA-seq defines trophoblast cell populations present in rhesus**
1317 **macaque and human trophoblast organoids. (A, B),** UMAP of cell type clusters from four lines
1318 of rhesus macaque (rTOs, A, n=11,916 cells) and four lines of human (hTOs, D, n=15,776 cells)
1319 trophoblast organoids. Single-cell dataset generated from three unique lines of rTOs and four
1320 unique lines of hTOs. Cell types are denoted as follows: cytotrophoblasts (CTB), proliferative

cytotrophoblasts (CTB-p), extravillous trophoblasts (EVT), syncytiotrophoblasts (STB). Multiple clusters of one cell type are annotated using -number after the cell name. **(C, D),** Comparison of the enrichment of distinct cell clusters in rTOs (C) and hTOs (D). **(E, F),** Dot plots showing expression levels of indicated genes in each cluster in rTOs (E) and hTOs (F). The indicated genes are established markers for the syncytiotrophoblast (STB), cytotrophoblasts (CTBs), extravillous trophoblasts (EVTs) and trophoblast progenitor cells (CTB-p). Scale is shown at bottom. **(G, H),** Feature plots of trophoblast marker gene expression in rTOs (G) or hTOs (H). Scale is shown at right.

Figure 3

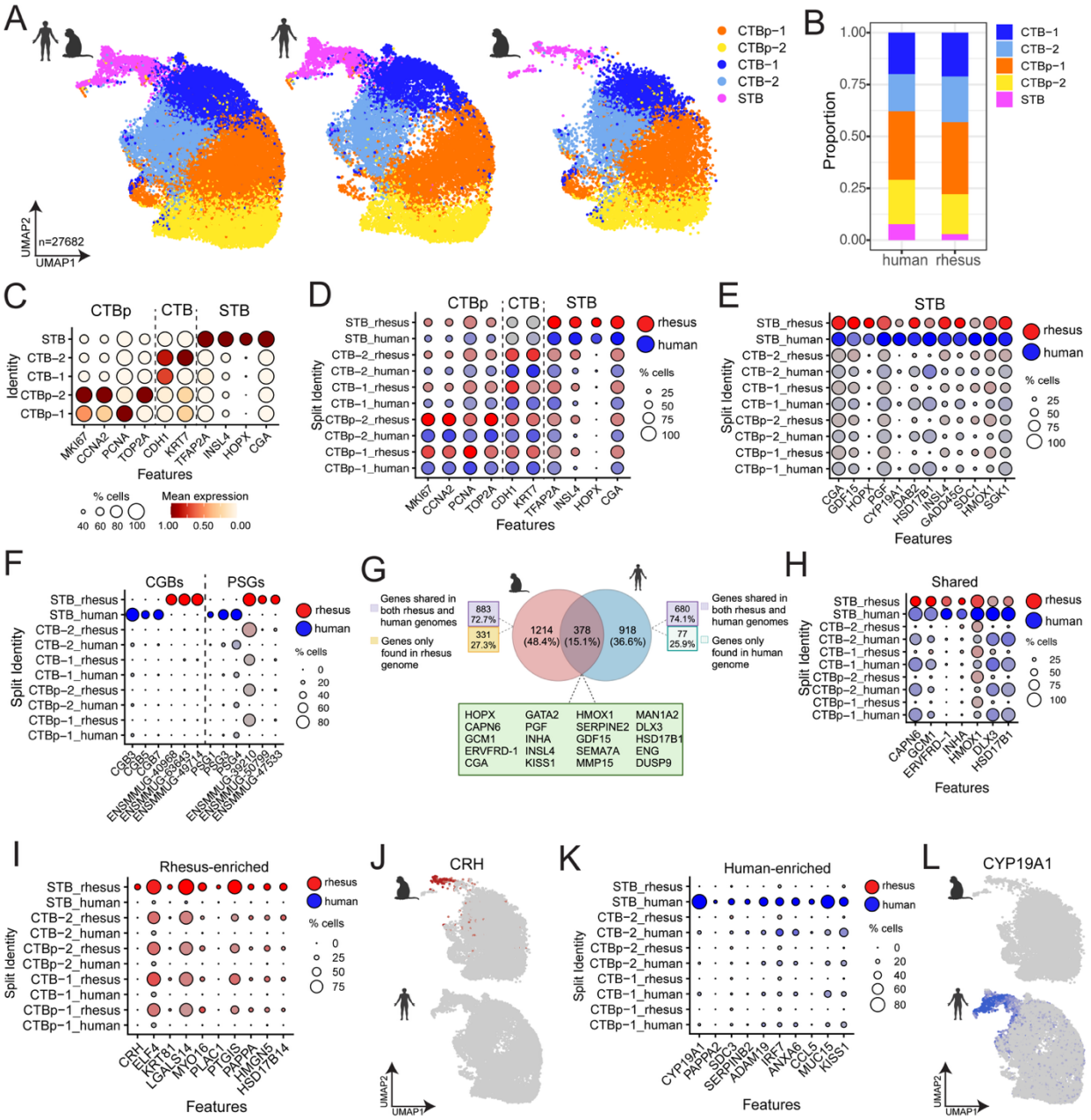

Figure 3. Integrated analysis of rhesus macaque and human single cell RNA-seq identifies shared and distinct cellular transcriptional profiles. (A), UMAP of merged cell type clusters from integrated datasets rTOs and hTOs (n=27,682 total cells). Three unique lines of rTOs and four unique lines of hTOs were used with four total samples from each species. Left, merged UMAP of clusters from rTOs and hTOs. Middle, cells from hTOs and right, cells from rTOs. **(B),** Cluster enrichment from hTO (left) and rTO (right) present in the integrated dataset. **(C),** Dot plots of canonical trophoblast markers in each cluster present in the integrated dataset. Key at bottom. **(D, E),** Canonical trophoblast markers in each cluster (D) or in the STB (E) present in the integrated dataset separated by species with rhesus in red and human in blue. Key at right. **(F),** Dot plots of rhesus macaque and human CGBs and PSGs (rhesus in red and human in blue). Key at right. **(G),** Venn diagram of markers in the rhesus and human STB clusters that identifies shared and distinct markers. Markers that were shared are shown as genes that are present in

both the rhesus macaque and human genome. Distinct rhesus and human STB markers include genes that are shared in the rhesus macaque and human genome as well as genes that are specific to one genome. **(H, I, J, K, L),** Dot plots of shared (H), rhesus-enriched (I) or human-enriched (K) markers found in the STB cluster separated by rTO and hTO conditions (rhesus in red and human in blue). Feature plot of CRH (J) and CYP19A1 (L) separated by rTO and hTO conditions.

1437 **Figure 4**

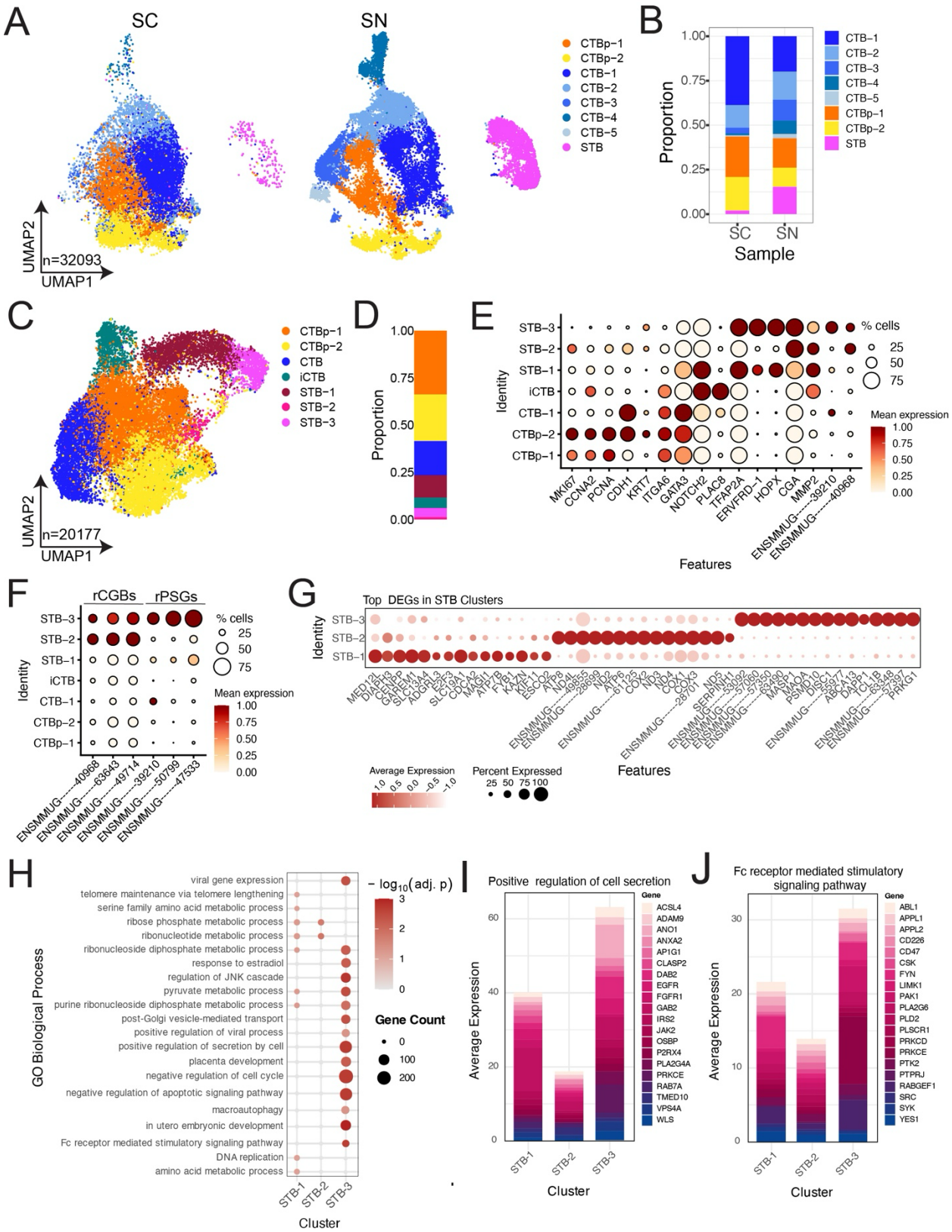

1438

Figure 4. Single-nucleus RNA Sequencing captures the full diversity of trophoblast cellular and transcriptional profile of rhesus macaque and human trophoblast organoids.
(A), UMAP of integrated datasets of rTO single-cell (SC) and single-nucleus (SN) RNA sequencing (n= 32,093 total cells/nuclei). Single-cell dataset generated from four rTO samples (SC, left) and single-nucleus generated from three rTO samples (SN, right). **(B),** Enrichment of cell clusters in SC (left) and SN (right). **(C),** UMAP of rTO SN dataset (n= 20,177 nuclei) created from three unique rTO lines. Seven clusters were identified, and cell types were indicated as follows: proliferative cytotrophoblasts (CTB-p), cytotrophoblasts (CTB), invasive cytotrophoblasts (iCTB), syncytiotrophoblast (STB). **(D),** Enrichment of cell clusters in rTO SN dataset depicted as a bar plot. **(E),** Dot plot depicting the expression levels of trophoblast markers shown in each cluster. Key at right. **(F),** Dot plot of rhesus CGBs and PSGs expression in each cluster. Key at right. **(G),** Dot plot of top differentially expressed genes in STB clusters. Key at bottom. **(H),** Dot plot of pathways from GO enrichment in STB clusters. Key at right. **(I, J),** Bar plots illustrating average expression of genes associated with positive regulation of cell secretion pathway (I) and Fc receptor mediated stimulatory signaling pathway in STB clusters.

Figure 5

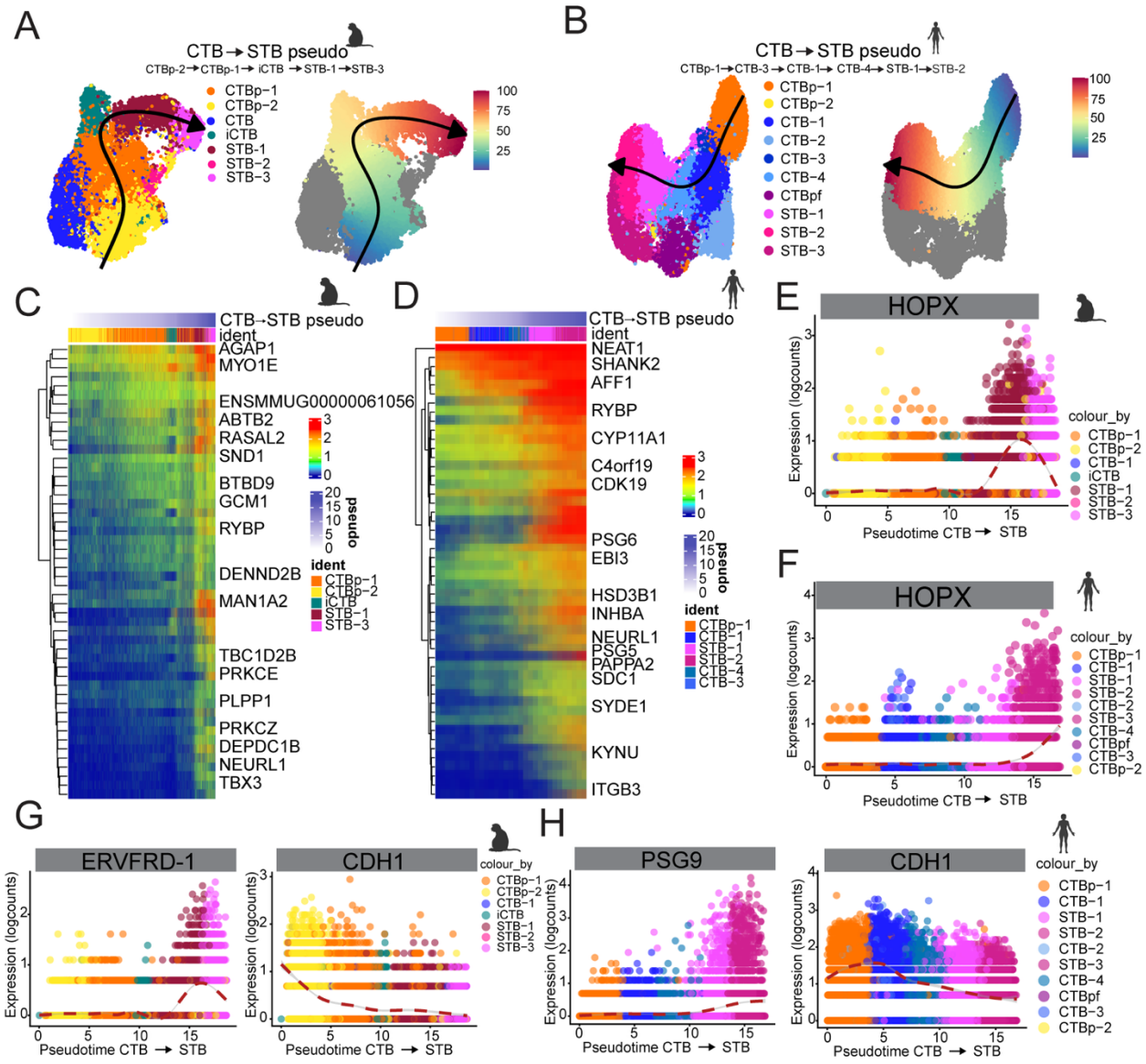

Figure 5. Inter-species profiling of rhesus macaque and human syncytiotrophoblast trajectory in sn-RNAseq datasets. (A, B), To analyze cellular lineage of trophoblast in rTOs and hTOs, pseudotime was implemented to visualize the trajectory of trophoblast cell types rTO (A, right) and hTO (B, right). Pseudotime values were assigned to each cell type and input into a color scale matching the UMAP based on time 0-100 in rTO (A, left) and hTO (B, left). The arrow across the UMAP shows the order of the trajectory. Pseudotime values revealed top genes correlated to the trajectory in rTO (A, right)and hTO (B, right). **(C, D),** Heatmap of the top increasing genes associated with the STB trajectory enriched in rTO (C) and hTO (D) dataset. **(E, F),** Increase of HOPX gene expression along the differentiation trajectory to STB subtype in rTO (E) and hTO (F). The cell types presented are represented by the colors denoted in the legend. Logcounts and pseudotime values are shown as a color scale present in the legend. **(G),** Normalized expression of ERVFRD-1and CDH1 shown along rTO pseudotime. **(H),** Normalized expression of PSG9 and CDH1 shown along hTO pseudotime.

1507 **Figure 6**

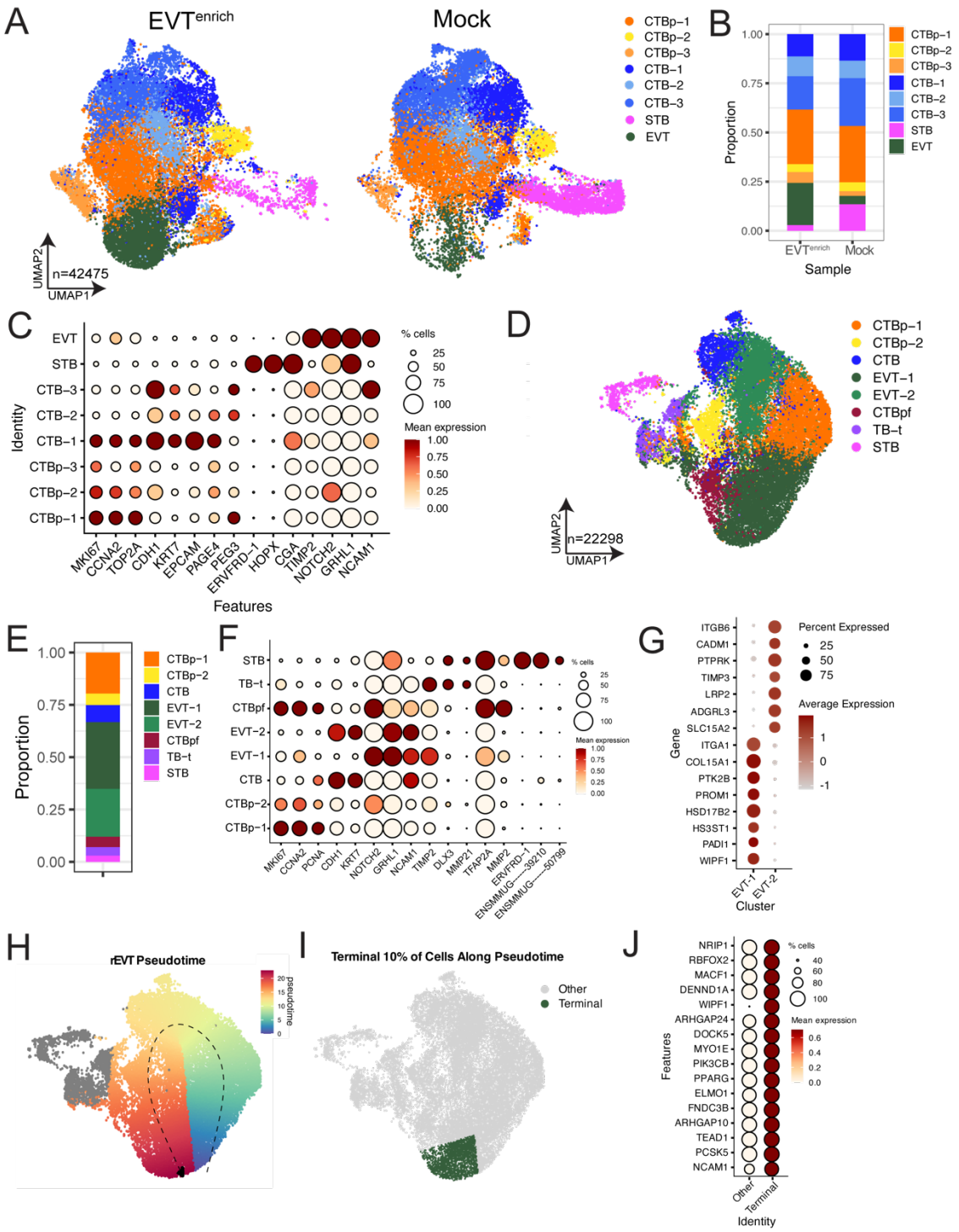

1508

1509 **Figure 6. Single-nucleus RNA-seq reveals extent of EVT differentiation in rTOs.** Three
1510 unique lines of rTOs induced to differentiate into EVTs (EVT^{enrich}) were submitted for sn-RNAseq.
1511 **(A),** UMAP of merged datasets of EVT^{enrich} and mock samples (n= 42,475 total nuclei). **(B),**
1512 Enrichment of trophoblast cell types in integrated EVT^{enrich} and mock dataset. **(C),** Dot plot
1513 illustrating gene expression of indicated trophoblast markers. Key at right. **(D),** UMAP of cell type
1514 clusters from EVT^{enrich} rhesus trophoblast organoids (n= 22,298 nuclei). Eight clusters were
1515 identified including two proliferative cytotrophoblast clusters (CTBp-1, CTBp-2), one

cytotrophoblast cluster (CTB), two extravillous trophoblast clusters (EVT-1, EVT-2), one cytotrophoblast pre-fusion cluster (CTBpf), one transitional population (tTB), and one syncytiotrophoblast cluster (STB). **(E),** Bar plot depicting enrichment of cell type clusters in EVT^{enrich} samples. **(F),** Dot plots of gene enrichment of trophoblast cell markers in EVT^{enrich} samples. **(G),** Dot plot of differentially expressed genes in EVT clusters. Key at right. **(H),** Pseudotime analysis revealed the cellular trajectory to the EVT-1 cluster. Feature plot of the pseudotime values assigned to each cell type and input into a color scale matching the UMAP based on time 0-100 EVT^{enrich} samples. **(I),** Feature plot of the terminal 10% of cells in the EVT trajectory shown in green. **(J),** Dot plot of enriched genes expressed in the terminal cells in the EVT trajectory. Key at right.

Figure 7

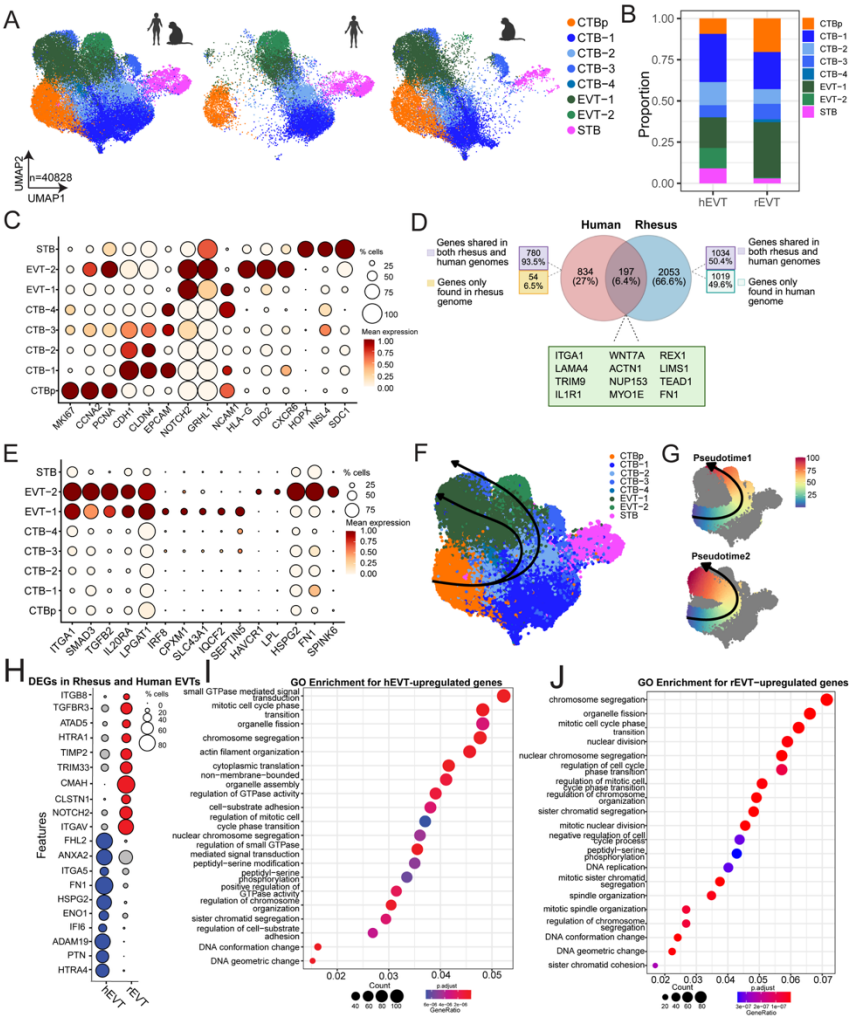

Figure 7. Integrated Analysis of EVT-enriched rTOs and hTOs. (A), UMAP of merged datasets of EVT^{enrich} rTO and EVT^{enrich} hTO datasets (n= 40,828 total nuclei). Three unique lines of EVT^{enrich} rTOs and three unique lines of EVT^{enrich} hTOs were used for analysis. Left, merged UMAP of clusters from EVT^{enrich} rTOs and EVT^{enrich} hTOs. Middle, cells from EVT^{enrich} hTOs and right, cells from EVT^{enrich} rTOs. **(B),** Enrichment of trophoblast cell types in integrated EVT^{enrich} datasets. **(C),** Dot plot illustrating gene expression of indicated trophoblast markers. Key at right. **(D),** Venn diagram of markers in the EVT^{enrich} rTO and EVT^{enrich} hTO EVT clusters that identifies shared and distinct markers. Markers that were shared are shown as genes that are present in both the rhesus macaque and human genome. Distinct rhesus and human EVT markers include genes that are shared in the rhesus macaque and human genome as well as genes that are specific to one genome. **(E),** Dot plot of enriched genes in EVT clusters in integrated dataset. **(F, G),** Pseudotime analysis of the merged of EVT^{enrich} rTO and EVT^{enrich} hTO datasets. The trajectory was mapped onto the UMAP, with pseudotime values assigned to each cell. (G) These values were then visualized using a color scale corresponding to pseudotime progression from 0 to 100 across the integrated dataset. **(H),** EVT cells were subsetted from the integrated dataset for further analysis of the EVT population. Dot plot of differentially expressed genes in rhesus and human EVTs. Key at right. **(I, J),** Dot plots of biological processes identified by differential expression between rhesus and human EVTs. GO enrichments for upregulated genes in human EVTs (I) and in rhesus EVTs (J). Key at bottom.

Figure S1

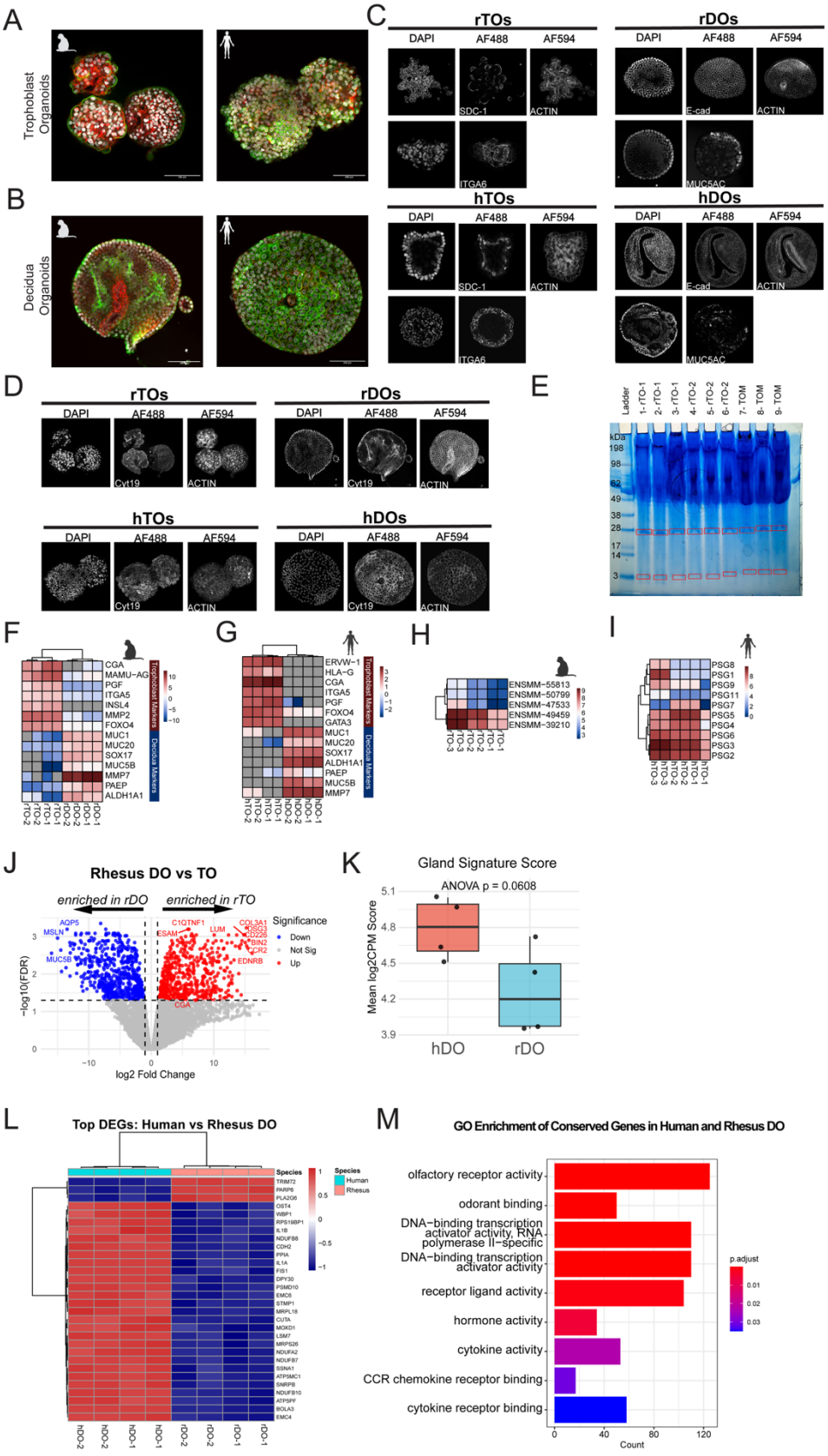
A
Trophoblast Organoids
B
Decidua Organoids
C
rTOs
rDOs
hTOs
hDOs
DAPI
AF488
AF594
SDC-1
ACTIN
ITGA6
E-cad
MUC5AC
D
Cyt19
E
Ladder
1- rTO-1
2- rTO-1
3- rTO-1
4- rTO-2
5- rTO-2
6- rTO-2
7- TOM
8- TOM
9- TOM
kDa
198
98
62
49
38
28
17
14
3
F
CGA
MAMU-AG
PGF
ITGA5
INSL4
MMP2
FOXO4
MUC1
MUC20
SOX17
MUC5B
MMP7
PAEP
ALDH1A1
Trophoblast Markers
Decidua Markers
G
ERVW-1
HLA-G
GATA3
H
ENSMM-55813
ENSMM-50799
ENSMM-47533
ENSMM-49459
ENSMM-39210
I
PSG8
PSG1
PSG9
PSG11
PSG7
PSG5
PSG4
PSG6
PSG3
PSG2
J
Rhesus DO vs TO
enriched in rDO
enriched in rTO
AQP5
MSLN
MUC5B
C1QTNF1
ESAM
LUM
COL3A1
DSG3
CD226
SIN2
CR2
EDNRB
CGA
Significance
Down
Not Sig
Up
−log10(FDR)
log2 Fold Change
K
Gland Signature Score
ANOVA p = 0.0608
Mean log2CPM Score
hDO
rDO
L
Top DEGs: Human vs Rhesus DO
Species
Human
Rhesus
M
GO Enrichment of Conserved Genes in Human and Rhesus DO
olfactory receptor activity
odorant binding
DNA−binding transcription activator activity, RNA polymerase II−specific
DNA−binding transcription activator activity
receptor ligand activity
hormone activity
cytokine activity
CCR chemokine receptor binding
cytokine receptor binding
p.adjust
Count

Supplemental Figure 1. Validation of rTOs and rDOs. (A, B), Confocal micrographs of rTOs (A) and hTOs (B) immunostained for CYT-19 (green), ACTIN (red), DAPI-stained nuclei are in black and white. Scale bar, 100μm. **(C),** Confocal micrographs of immunostained rTOs, hTOs, rDOs and hDOs in black and white. **(D),** Confocal micrographs of rDOs and hDOs immunostained for CYT-19 (green), ACTIN (red), DAPI-stained nuclei are in black and white. **(E),** SDS-PAGE gel of rTO CM samples. Red boxes indicate bands that were excised and used for mass spectrometry. **(F, G),** Heatmap (based on $\log_2$ RPKM values) of transcripts expressed in hDOs and hTOs (F) and rDOs and rTOs (G) that are associated with markers of trophoblasts and decidua. Data shown is 2 biological replicates and 2 technical replicates in rTOs and rDOs. **(H),** Heatmap (based on $\log_2$ RPKM values) of identified pregnancy- specific glycoproteins (PSGs) transcripts expressed in rTOs. Data shown is 3 biological replicates and 2 technical replicates in rTOs. **(I),** Heatmap (based on $\log_2$ RPKM values) of known pregnancy-specific glycoproteins (PSGs) transcripts expressed in hTOs. Key at right. Red indicates high levels of expression; blue indicates low levels of expression. Data shown is 3 biological replicates and 2 technical replicates in hTOs. **(J),** Volcano plot of differentially expressed transcripts in rTOs and rDOs. Red circles represent transcripts significantly upregulated and blue circles represent transcripts significantly downregulated ($\log_2$fold-change > $\pm$ 1 and FDR < 0.05) and gray circles represent transcripts that were not significantly changed. **(K),** Boxplot of gland signature score in hDOs and rDOs determined by glandular epithelial markers. **(L),** Heatmap of top differentially expressed genes in hDOs and rDOs. Key at right, red indicates high levels of expression and blue indicates low levels of expression. **(M),** Bar plot of GO enrichment terms associated with conserved genes in hDOs and rDOs. Key at right.

Figure S2

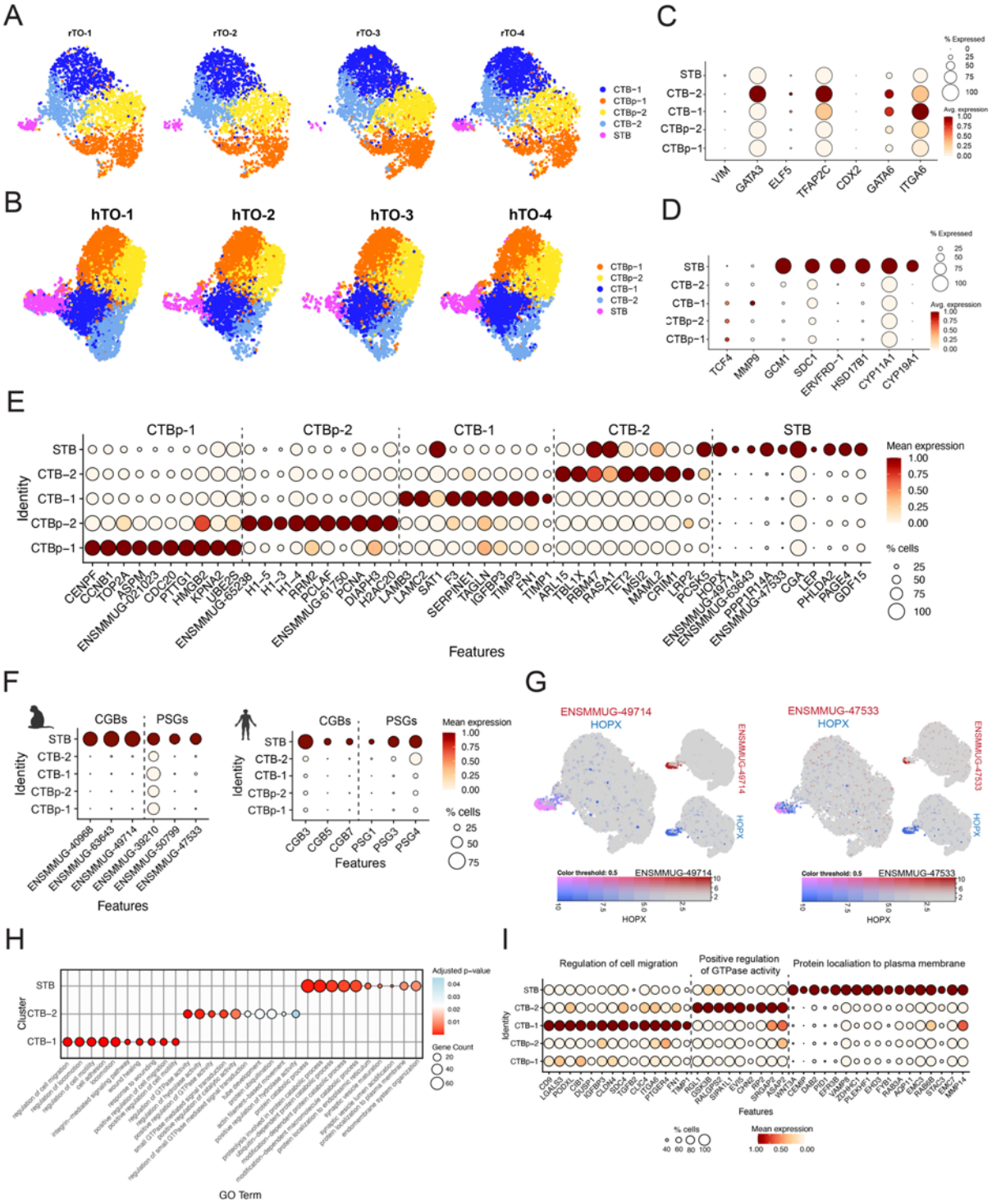

Supplemental Figure 2. Defining cell types in rTO and hTO sc-RNAseq datasets. Individual UMAPs from samples of **(A)** Four rTO samples and **(B)** Four hTO samples. Dot plots of gene expression of **(C)** cytotrophoblast markers and **(D)** syncytiotrophoblast or extravillous trophoblast markers in rTOs. **(E),** Dot plot of top 10 markers in each cluster in rTOs. Key at right. **(F),** Dot plot of rhesus CGBs and PSGs in rTOs (left) and human CGBs and PSGs in hTOs (right). Key at right.

(G), Combined feature plots of rhesus CGB (ENSMMUG00000049714) and HOPX (left) and rhesus PSG (ENSMMUG00000047533) and HOPX (right) in rTOs. Key at bottom. **(H),** Top biological processes for CTB-1, CTB-2, and STB clusters in rTOs identified using ClusterProfiler. **(I),** Dot plots of genes associated with top biological processes in CTB-1, CTB-2 and STB clusters in rTOs.

Figure S3

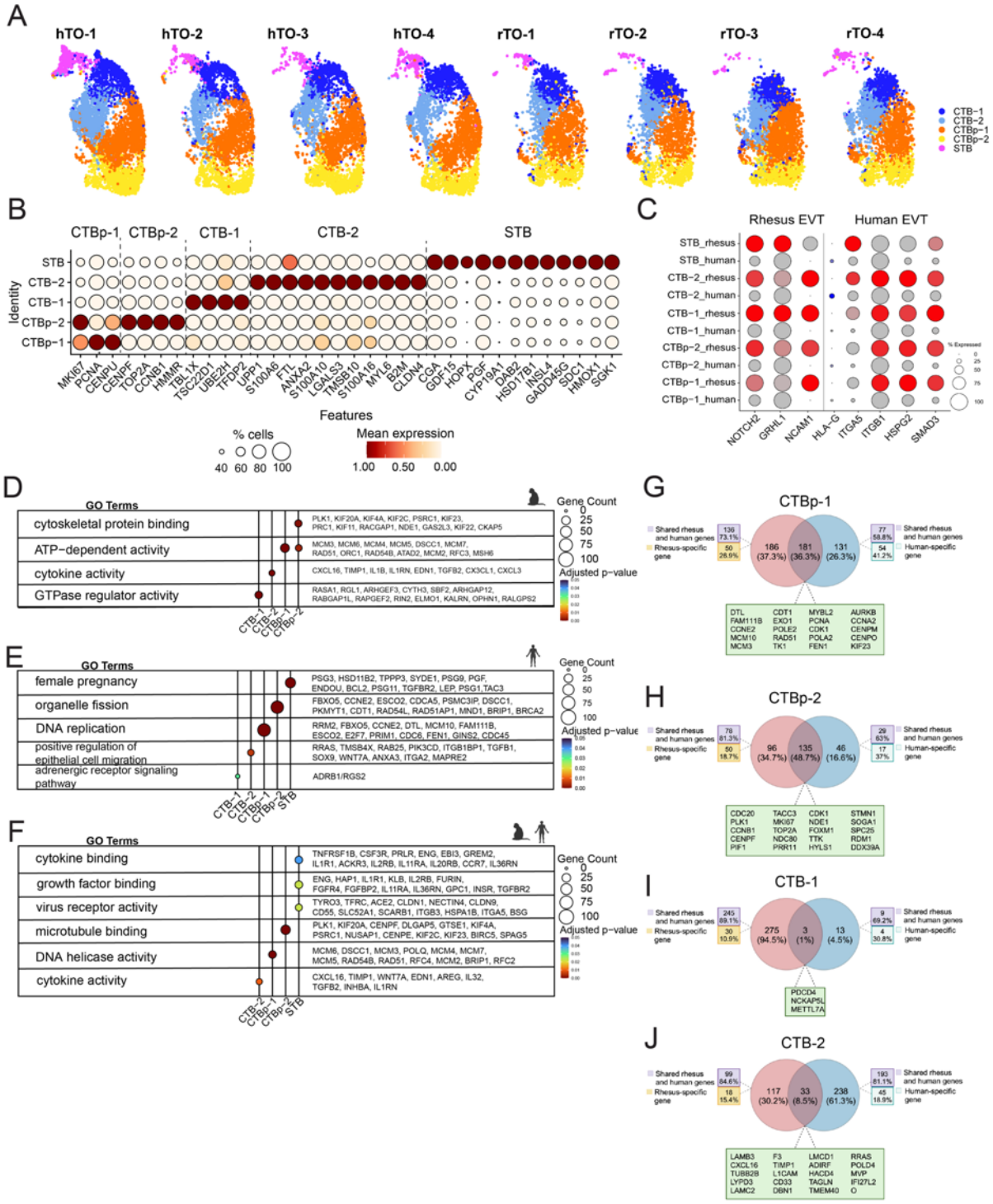

Supplemental Figure 3. Defining cell types in integrated sc-RNAseq dataset with rTO and hTO. (A), Individual UMAP of hTO and rTO samples that comprise that integrated dataset. **(B),** Dot plot of gene expression of cytotrophoblasts, proliferative cytotrophoblasts, and

syncytiotrophoblasts. **(C),** Dot plot of rhesus macaque and human extravillous trophoblast markers in the integrated dataset (rhesus are shown in red and human shown in blue). **(D, E, F),** Subset of pathways from GO term enrichment in all clusters in subsetted (D) rTO dataset and (E) hTO (F) integrated rTO and hTO dataset. Venn diagram of markers in the rhesus and human **(G),** CTBp-1, **(H),** CTBp-2, **(I),** CTB-1, **(J),** CTB-2 clusters that identifies shared and distinct markers. Markers that were not shared are shown as genes that are present in both the rhesus macaque and human genome as well as markers that are specific to one genome.

Figure S4

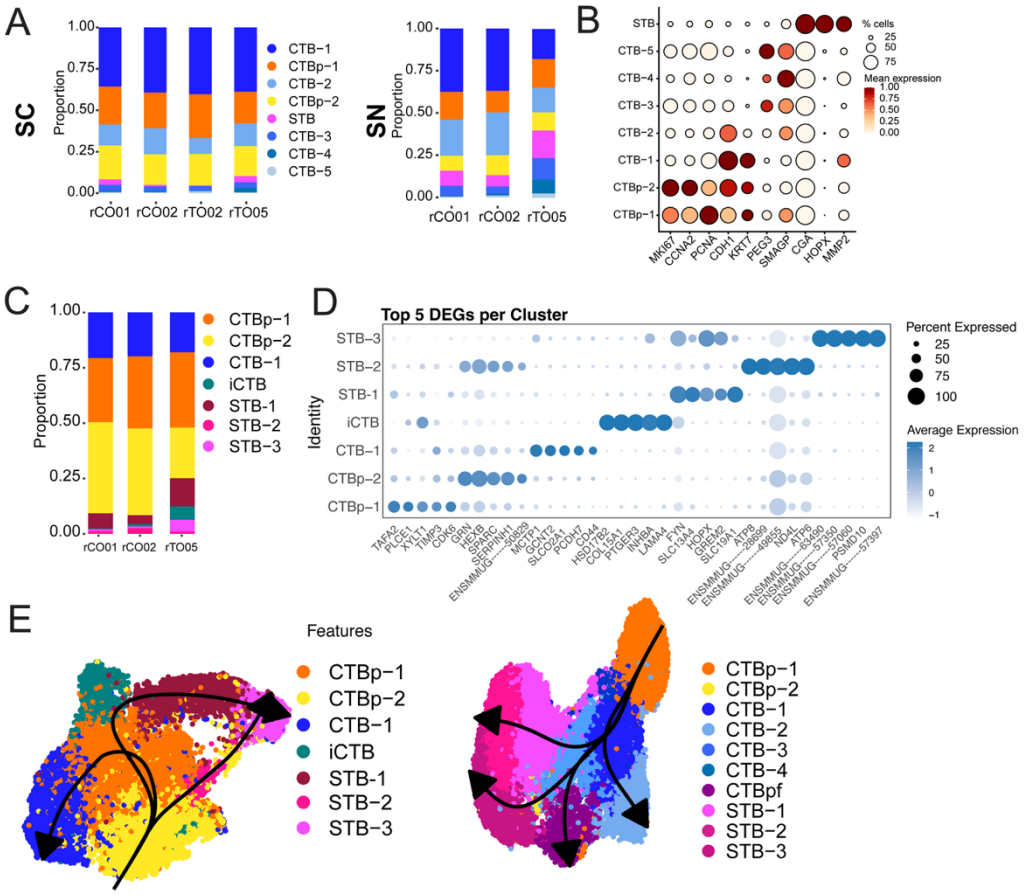

Supplemental Figure 4. Defining cell types in rTO sn-RNAseq and integrated sn-RNAseq and sc-RNAseq datasets. (A), Individual bar plots showing enrichment of cell types in sc-RNAseq (SC) samples (left) and sn-RNAseq (SN) samples (right). **(B),** Dot plot of expression of canonical trophoblast markers in integrated SC and SN dataset. **(C),** Cell type enrichment of individual rTO samples. **(D),** Dot plot of top five differentially expressed genes per cluster in rTO sn-RNAseq dataset. Key at right. **(E),** Pseudotime analysis of the rTO (F) and hTO (G) datasets. The trajectories were mapped onto their respective UMAPs.

Figure S5

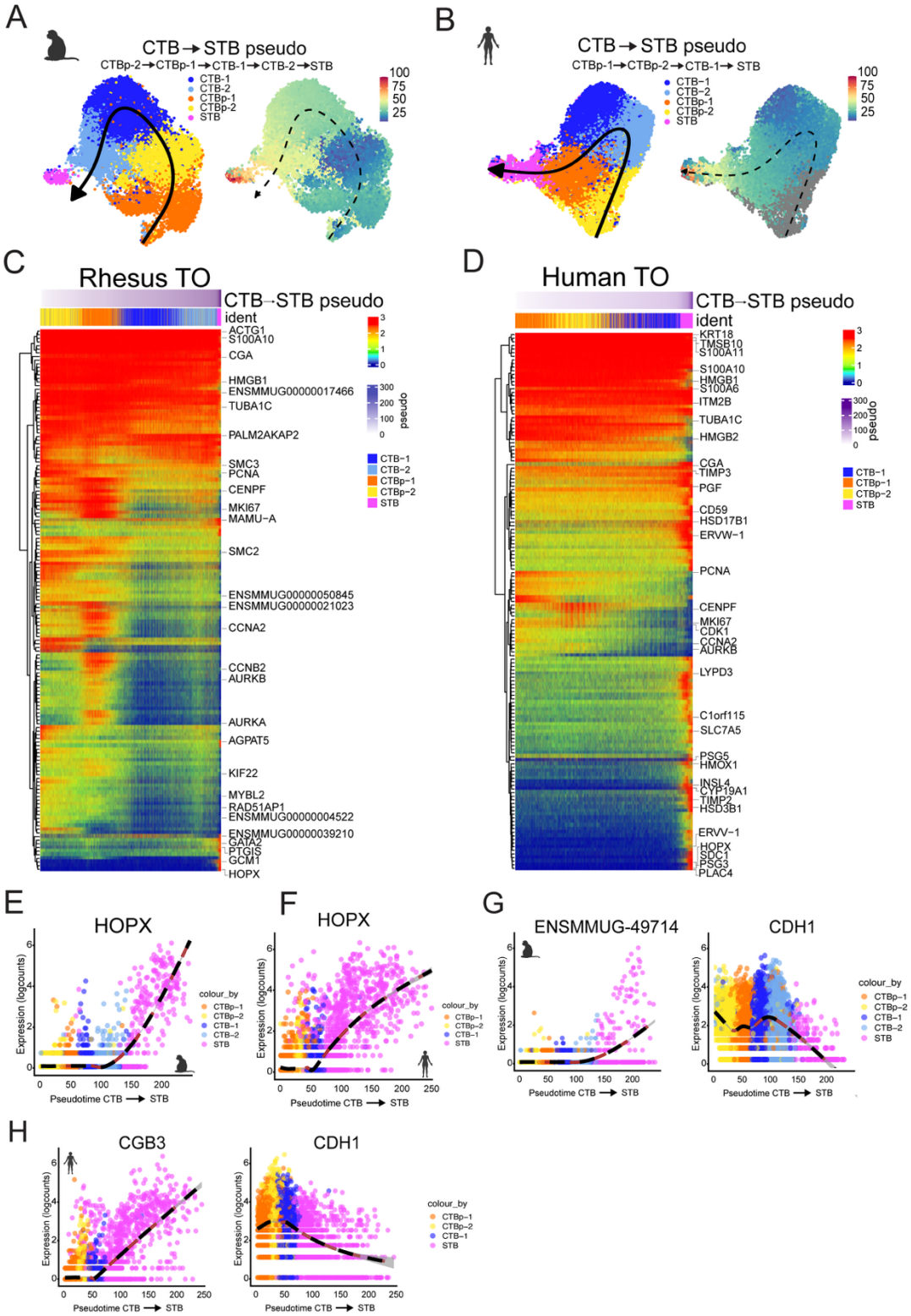

Supplemental Figure 5. Syncytiotrophoblast cell differentiation trajectory in rhesus and human trophoblast organoids.

(A,B), Pseudotime was performed using Slingshot analysis to define cellular lineage reconstruction across sc-RNAseq datasets. This illustrates the trajectory of the cell types in the

clusters in rTO (A, right) and hTO (B, right). Pseudotime values were assigned to each cell type and input into a color scale matching the UMAP based on time 0-100 in rTO (A, left) and hTO (B, left). The arrow across the UMAP shows the order of the trajectory. **(C, D),** Pseudotime values revealed top genes correlated to the trajectory in rTO (C) and hTO (D). **(E, F),** HOPX gene expression increases along the differentiation trajectory to STB subtype in rTO (E) and hTO (F). The cell types presented are represented by the colors denoted in the legend. Logcounts and pseudotime values are shown as a color scale present in the legend. **(G),** Normalized expression of ENSMMUG-49714and CDH1 shown along rTO pseudotime. **(H),** Normalized expression of CGB3 and CDH1 shown along hTO pseudotime.

Figure S6

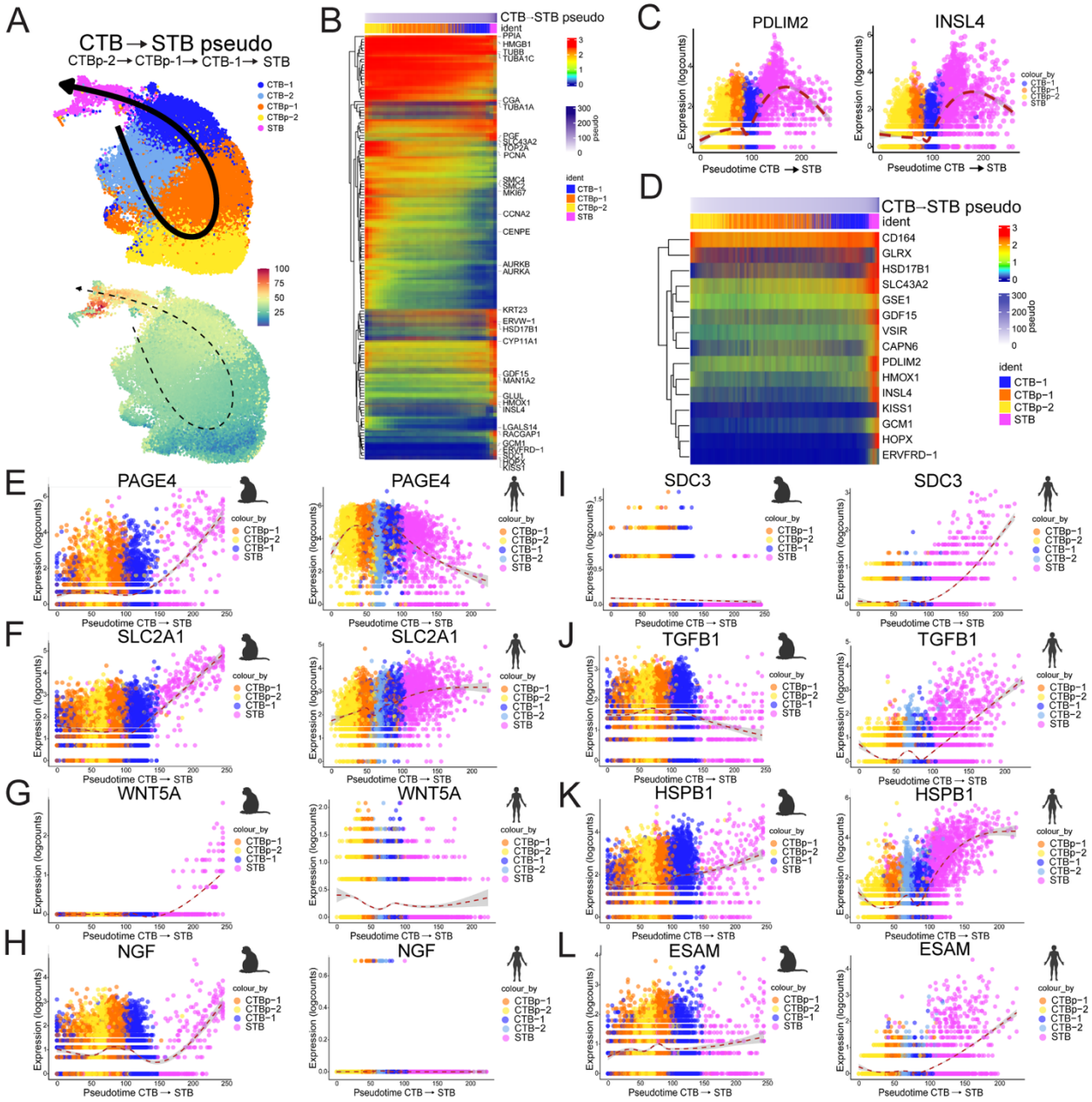

Supplemental Figure 6. Comparative single cell RNA-seq reveals distinct STB differentiation trajectories between human and rhesus macaque trophoblast organoids. **(A),** Pseudotime analysis of the integrated rTO and hTO datasets. The trajectory was mapped onto the UMAP, with pseudotime values assigned to each cell. These values were then visualized using a color scale corresponding to pseudotime progression from 0 to 100 across the integrated dataset. **(B),** Heatmap of the top genes associated with the pseudotime enriched in the combined rTO and hTO trajectory dataset. **(C),** Normalized expression of PDLIM2 and INSL4 shown along integrated pseudotime in the combined dataset. **(D),** Heatmap of genes that increase along the trajectory to the STB subtype in the integrated dataset. The cell types presented are represented by the colors denoted in the legend. Logcounts and pseudotime values are shown as a color scale present in the legend. **(E, F, G, H),** Normalized expression of PAGE4, SLC2A1, WNT5A, and NGF

shown across rTO (on left) and hTO (on right) trajectories. **(I, J, K, L),** Normalized expression of SDC3, TGFB1, HSPB1, and ESAM shown along rTO (on left) and hTO (on right) trajectories.

Figure S7

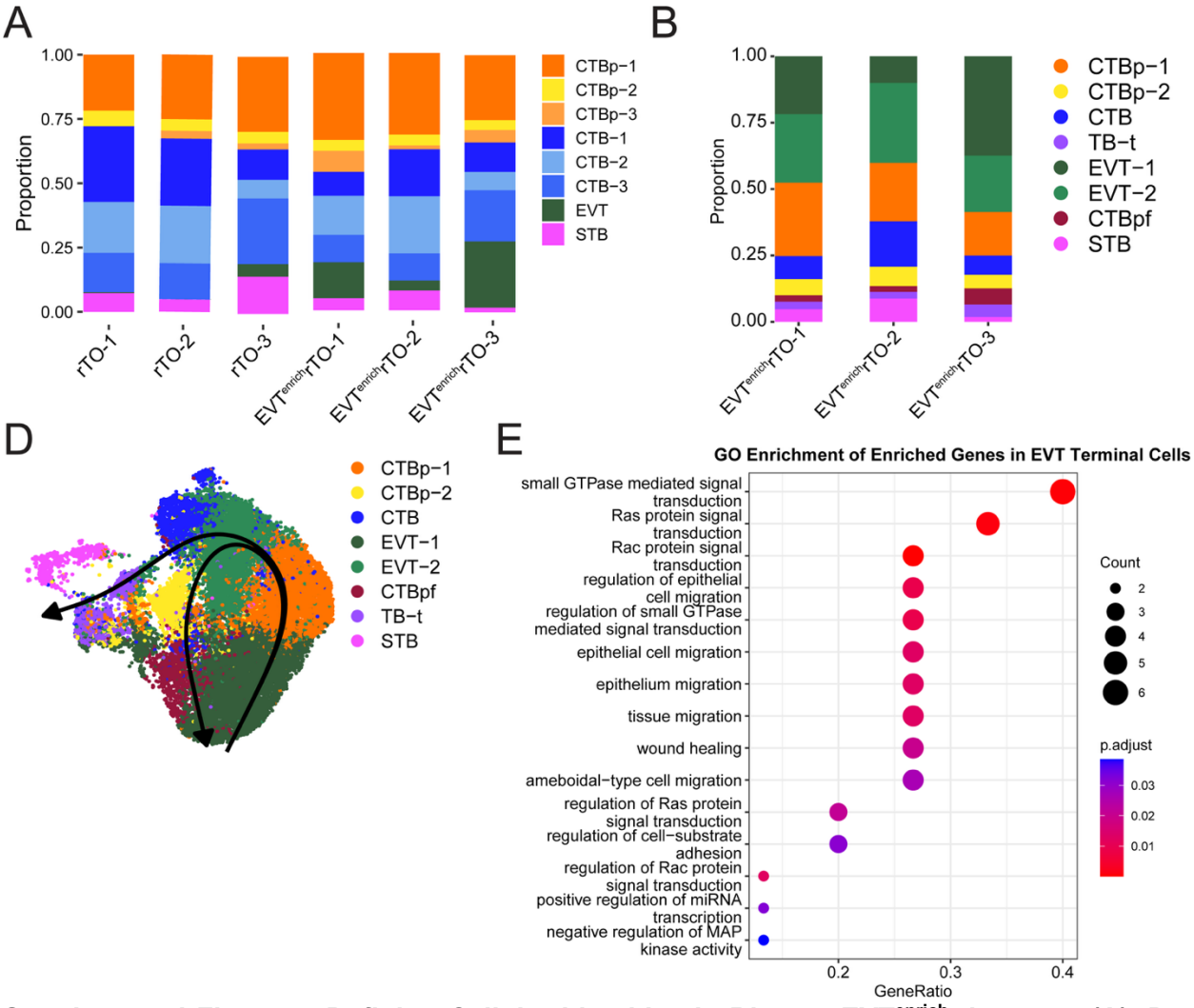

Supplemental Figure 7. Defining Cellular Identities in Rhesus EVT^{enrich} datasets. (A), Bar plots of cluster enrichment from integrated dataset of Mock and EVT^{enrich} samples. **(B),** Bar plots of cluster enrichment in EVT^{enrich} samples. **(C),** Pseudotime analysis of the EVT^{enrich} dataset. The trajectories were mapped onto the UMAP. **(D),** Dot plot of GO enrichment of enriched genes in 10% terminal cells in EVT trajectory compared to other cells.

1925 **Figure S8**

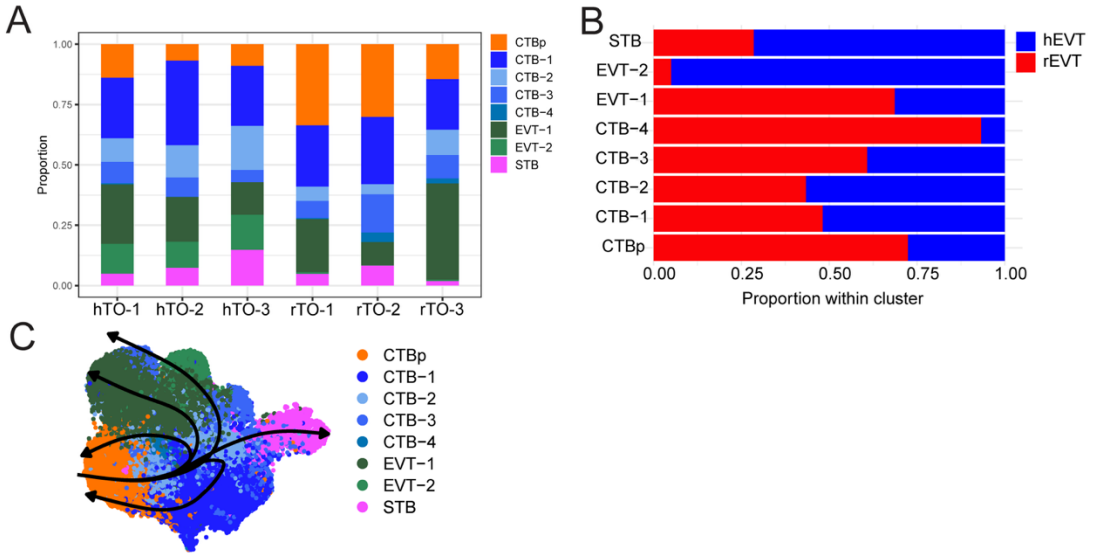

1926
1927 **Supplemental Figure 8. Defining Trophoblast Population in Integrated Human and Rhesus**
1928 **EVT^{enrich}. (A),** Cluster enrichment of individual samples in merged dataset. **(B),** Bar plot of
1929 proportion of cluster comprised of human (in blue) or rhesus nuclei (in red). **(C),** Pseudotime
1930 analysis of the integrated EVT^{enrich} dataset. The five trajectories were mapped onto the UMAP.
1931

1932

1933

1934

1935

1936

1937

1938

1939

1940

Supplemental Figure Legends

Supplemental Figure 1. Validation of rTOs and rDOs. (A, B), Confocal micrographs of rTOs (A) and hTOs (B) immunostained for CYT-19 (green), ACTIN (red), DAPI-stained nuclei are in black and white. Scale bar, 100μm. **(C),** Confocal micrographs of immunostained rTOs, hTOs, rDOs and hDOs in black and white. **(D),** Confocal micrographs of rDOs and hDOs immunostained for CYT-19 (green), ACTIN (red), DAPI-stained nuclei are in black and white. **(E),** SDS-PAGE gel of rTO CM samples. Red boxes indicate bands that were excised and used for mass spectrometry. **(F, G),** Heatmap (based on $\log_2$ RPKM values) of transcripts expressed in hDOs and hTOs (F) and rDOs and rTOs (G) that are associated with markers of trophoblasts and decidua. Data shown is 2 biological replicates and 2 technical replicates in rTOs and rDOs. **(H),** Heatmap (based on $\log_2$ RPKM values) of identified pregnancy- specific glycoproteins (PSGs) transcripts expressed in rTOs. Data shown is 3 biological replicates and 2 technical replicates in rTOs. **(I),** Heatmap (based on $\log_2$ RPKM values) of known pregnancy-specific glycoproteins (PSGs) transcripts expressed in hTOs. Key at right. Red indicates high levels of expression; blue indicates low levels of expression. Data shown is 3 biological replicates and 2 technical replicates in hTOs. **(J),** Volcano plot of differentially expressed transcripts in rTOs and rDOs. Red circles represent transcripts significantly upregulated and blue circles represent transcripts significantly downregulated ($\log_2$fold-change > $\pm$ 1 and FDR < 0.05) and gray circles represent transcripts that were not significantly changed. **(K),** Boxplot of gland signature score in hDOs and rDOs determined by glandular epithelial markers. **(L),** Heatmap of top differentially expressed genes in hDOs and rDOs. Key at right, red indicates high levels of expression and blue indicates low levels of expression. **(M),** Bar plot of GO enrichment terms associated with conserved genes in hDOs and rDOs. Key at right.

Supplemental Figure 2. Defining cell types in rTO and hTO sc-RNAseq datasets. Individual UMAPs from samples of **(A)** Four rTO samples and **(B)** Four hTO samples. Dot plots of gene expression of **(C)** cytotrophoblast markers and **(D)** syncytiotrophoblast or extravillous trophoblast markers in rTOs. **(E),** Dot plot of top 10 markers in each cluster in rTOs. Key at right. **(F),** Dot plot of rhesus CGBs and PSGs in rTOs (left) and human CGBs and PSGs in hTOs (right). Key at right. **(G),** Combined feature plots of rhesus CGB (ENSMMUG00000049714) and HOPX (left) and rhesus PSG (ENSMMUG00000047533) and HOPX (right) in rTOs. Key at bottom. **(H),** Top biological processes for CTB-1, CTB-2, and STB clusters in rTOs identified using ClusterProfiler. **(I),** Dot plots of genes associated with top biological processes in CTB-1, CTB-2 and STB clusters in rTOs.

Supplemental Figure 3. Defining cell types in integrated sc-RNAseq dataset with rTO and hTO. (A), Individual UMAP of hTO and rTO samples that comprise that integrated dataset. **(B),** Dot plot of gene expression of cytotrophoblasts, proliferative cytotrophoblasts, and syncytiotrophoblasts. **(C),** Dot plot of rhesus macaque and human extravillous trophoblast markers in the integrated dataset (rhesus are shown in red and human shown in blue). **(D, E, F),** Subset of pathways from GO term enrichment in all clusters in subsetted (D) rTO dataset and (E) hTO (F) integrated rTO and hTO dataset. Venn diagram of markers in the rhesus and human **(G),** CTBp-1, **(H),** CTBp-2, **(I),** CTB-1, **(J),** CTB-2 clusters that identifies shared and distinct markers. Markers that were not shared are shown as genes that are present in both the rhesus macaque and human genome as well as markers that are specific to one genome.

Supplemental Figure 4. Defining cell types in rTO sn-RNAseq and integrated sn-RNAseq and sc-RNAseq datasets. (A), Individual bar plots showing enrichment of cell types in sc-RNAseq (SC) samples (left) and sn-RNAseq (SN) samples (right). **(B),** Dot plot of expression of canonical trophoblast markers in integrated SC and SN dataset. **(C),** Cell type enrichment of

individual rTO samples. **(D),** Dot plot of top five differentially expressed genes per cluster in rTO sn-RNAseq dataset. Key at right. **(E),** Pseudotime analysis of the rTO (F) and hTO (G) datasets. The trajectories were mapped onto their respective UMAPs.

Supplemental Figure 5. Syncytiotrophoblast cell differentiation trajectory in rhesus and human trophoblast organoids.
(A,B), Pseudotime was performed using Slingshot analysis to define cellular lineage reconstruction across sc-RNAseq datasets. This illustrates the trajectory of the cell types in the clusters in rTO (A, right) and hTO (B, right). Pseudotime values were assigned to each cell type and input into a color scale matching the UMAP based on time 0-100 in rTO (A, left) and hTO (B, left). The arrow across the UMAP shows the order of the trajectory. **(C, D),** Pseudotime values revealed top genes correlated to the trajectory in rTO (C) and hTO (D). **(E, F),** HOPX gene expression increases along the differentiation trajectory to STB subtype in rTO (E) and hTO (F). The cell types presented are represented by the colors denoted in the legend. Logcounts and pseudotime values are shown as a color scale present in the legend. **(G),** Normalized expression of ENSMMUG-49714and CDH1 shown along rTO pseudotime. **(H),** Normalized expression of CGB3 and CDH1 shown along hTO pseudotime.

Supplemental Figure 6. Comparative single cell RNA-seq reveals distinct STB differentiation trajectories between human and rhesus macaque trophoblast organoids.
(A), Pseudotime analysis of the integrated rTO and hTO datasets. The trajectory was mapped onto the UMAP, with pseudotime values assigned to each cell. These values were then visualized using a color scale corresponding to pseudotime progression from 0 to 100 across the integrated dataset. **(B),** Heatmap of the top genes associated with the pseudotime enriched in the combined rTO and hTO trajectory dataset. **(C),** Normalized expression of PDLIM2 and INSL4 shown along integrated pseudotime in the combined dataset. **(D),** Heatmap of genes that increase along the trajectory to the STB subtype in the integrated dataset. The cell types presented are represented by the colors denoted in the legend. Logcounts and pseudotime values are shown as a color scale present in the legend. **(E, F, G, H),** Normalized expression of PAGE4, SLC2A1, WNT5A, and NGF shown across rTO (on left) and hTO (on right) trajectories. **(I, J, K, L),** Normalized expression of SDC3, TGFB1, HSPB1, and ESAM shown along rTO (on left) and hTO (on right) trajectories.

Supplemental Figure 7. Defining Cellular Identities in Rhesus EVT^{enrich} datasets. (A), Bar plots of cluster enrichment from integrated dataset of Mock and EVT^{enrich} samples. **(B),** Bar plots of cluster enrichment in EVT^{enrich} samples. **(C),** Pseudotime analysis of the EVT^{enrich} dataset. The trajectories were mapped onto the UMAP. **(D),** Dot plot of GO enrichment of enriched genes in 10% terminal cells in EVT trajectory compared to other cells.

Supplemental Figure 8. Defining Trophoblast Population in Integrated Human and Rhesus EVT^{enrich}. (A), Cluster enrichment of individual samples in merged dataset. **(B),** Bar plot of proportion of cluster comprised of human (in blue) or rhesus nuclei (in red). **(C),** Pseudotime analysis of the integrated EVT^{enrich} dataset. The five trajectories were mapped onto the UMAP.

Supplemental Table Legends

Supplemental Table 1. Metadata of animal study design.
Supplemental Table 2. Metadata of trophoblast organoid lines.
Supplemental Table 3. Components of term trophoblast organoid (tTOM) media.
Supplemental Table 4. Components of decidua organoid media.
Supplemental Table 5. Components of EVT differentiation media 1.
Supplemental 6. Components of EVT differentiation media 2.
Supplemental Table 7. Antibodies used for immunofluorescence staining.

Supplemental Table 8. Significant Genes along STB trajectory in rTO snRNAseq dataset. Genes with significant association to STB lineage trajectory identified using *associationTest()* in R. False Discovery rate (FDR) and adjusted p-value <0.05 were used to determined significant genes. These genes reflect the transcriptional changes throughout the developmental trajectory.

Supplemental Table 9. Significant Genes along STB trajectory in rTO scRNAseq dataset. Genes with significant association to STB lineage trajectory identified using *associationTest()* in R. False Discovery rate (FDR) and adjusted p-value <0.05 were used to determined significant genes. These genes reflect the transcriptional changes throughout the developmental trajectory.

Supplemental Table 10. Significant Genes along STB trajectory in hTO snRNAseq dataset. Genes with significant association to STB lineage trajectory identified using *associationTest()* in R. False Discovery rate (FDR) and adjusted p-value <0.05 were used to determined significant genes. These genes reflect the transcriptional changes throughout the developmental trajectory.

Supplemental Table 11. Significant Genes along STB trajectory in hTO scRNAseq dataset. Genes with significant association to STB lineage trajectory identified using *associationTest()* in R. False Discovery rate (FDR) and adjusted p-value <0.05 were used to determined significant genes. These genes reflect the transcriptional changes throughout the developmental trajectory.

Supplemental Movie Legends

Supplemental Movie 1. Three-dimensional reconstruction of rhesus trophoblast organoid. Rhesus trophoblast organoids were fixed and immunostained for SDC-1 (green), a marker of syncytiotrophoblasts, and actin (red) to visualize cellular architecture. Nuclei were counterstained with DAPI (blue). Z-stack images were acquired by confocal microscopy and reconstructed into a three-dimensional rendering using Imaris software. The movie illustrates the complex organization and surface morphology of the organoids in three dimensions.

Supplemental Movie 2. Three-dimensional reconstruction of rhesus decidua gland organoid. Rhesus decidua gland organoids were fixed and immunostained for E-cadherin (green) and actin (red) to visualize cellular architecture. Nuclei were counterstained with DAPI (blue). Z-stack images were acquired by confocal microscopy and reconstructed into a three-dimensional rendering using Imaris software. The movie illustrates the complex organization and surface morphology of the organoids in three dimensions.